



**Large-scale unsteadiness in a compression ramp flow confined by sidewalls**Akshay S. Deshpande \* and Jonathan Poggie †  
Purdue University, West Lafayette, Indiana 47906, USA

(Received 19 June 2020; accepted 3 February 2021; published 26 February 2021)

Conventional shock-wave–turbulent boundary-layer interactions are often treated as quasi-two dimensional for a tractable analysis. In practical applications such as high-speed engine inlets and combustors, the additional presence of sidewalls leads to dramatic changes in the baseline flow structure by enhancing the inherent three dimensionality of the interaction, in addition to modifying its unsteadiness. This study investigates the flow field generated by a  $24^\circ$  compression ramp in presence of sidewalls, with a confinement ratio  $\delta/w = 0.12$ . The free-stream unit Reynolds number and Mach number are  $2.5 \times 10^7 \text{ m}^{-1}$  and 2.25, respectively. Statistical analysis of results obtained from high-fidelity simulations carried out by Poggie and Porter [*Phys. Rev. Fluids* 4, 024602 (2019)] is performed to explore the large-scale unsteadiness of this flow field. The mean and instantaneous flow fields displayed strong three dimensionality due to influence of sidewalls. Fourier analysis of wall-pressure data revealed frequency bands typically associated with low-frequency shock oscillations,  $St \approx O(0.01)$ , as well as vortex shedding occurring at mid frequencies,  $St \approx O(0.1)$ . The spectra of shock oscillations and separation bubble breathing indicated a dominant low- and mid-frequency component, respectively, akin to a quasi-two-dimensional shock-induced separation. The centerline shock oscillations were well correlated with the breathing motion of the centerline separation bubble, as well as turbulence in the upstream boundary layer. Effects of sidewalls on the overall unsteadiness were investigated by estimating coherence and correlations between various quantities. Plots of coherence between shock motion and pressure fluctuations in the domain indicated asymmetric motion of the interaction, possibly caused by alternating breathing motion of the separated zones on the sidewalls. Space-time correlations on the floor suggested a strong influence of centerline separation on the corner separations and vice versa. Similar correlations with left and right sidewalls confirmed the asymmetric motion of the interaction with a frequency of  $St \approx 0.026$ .

DOI: [10.1103/PhysRevFluids.6.024610](https://doi.org/10.1103/PhysRevFluids.6.024610)**I. INTRODUCTION**

Considerable progress has been made in understanding the phenomenon of shock-wave–turbulent boundary-layer interactions (SWTBLI) [1–4]. Novel experimental techniques and high-speed wind tunnels have enabled researchers to study the dynamics of SWTBLI in complex configurations. Additionally, design of efficient numerical algorithms, with controlled dissipation, has allowed detailed insights into the flow physics by enabling sufficient spatial and temporal resolution. The majority of this research has leveraged a two-dimensional approximation, either by taking measurements on the centerline or using aerodynamic fences in experiments, and using periodic boundary conditions in case of computations for a tractable analysis.

\*deshpan2@purdue.edu

†jpoggie@purdue.edu

An extensive body of literature is dedicated to examining the causes of unsteadiness in a SWTBLI, mostly under the quasi-two-dimensional assumption. Using statistical analysis, it was observed that for interactions with attached or moderately separated flow, the shock responds to upstream fluctuations at frequencies approximately two orders of magnitude lower than that characterizing the incoming turbulence. In case of massively separated flows, downstream events such as periodic vortex shedding and breathing motion of the separated zone modulate the shock motion [3]. Additional features of unsteadiness in a SWTBLI were discovered by employing reduced order modeling and linear stability analysis. Nichols *et al.* [5] used dynamic mode decomposition (DMD) to describe two modes corresponding to the low-frequency breathing motion of the separation bubble and high-frequency propagation of instability waves. Modes obtained via global linear stability analysis were consistent with the DMD modes, as well as suggesting that the shock and bubble system acts like a weakly damped oscillator sustained by upstream forcing. Adler and Gaitonde [6] performed a perturbation analysis and determined an absolute instability which was self-sustaining, but unaffected by external forcing. Specific events such as mid-frequency Kelvin-Helmholtz shedding, low mid-frequency separation bubble oscillations, and low-frequency shock motion characterized the dynamics of SWTBLI.

In aircraft components such as inlets and nozzles (operating at off-design conditions), the presence of additional no-slip boundaries exacerbates the inherent three dimensionality of a SWTBLI by increasing the extent of the separated regions. Using a quasi-two-dimensional approximation in such instances leads to errors in prediction of critical aerodynamic quantities such as heat transfer at the wall and skin-friction coefficient. The influence of additional no-slip boundaries on the flow field has been studied both experimentally [7–13] and computationally [14–18]. Reda and Murphy [7,8] investigated the effects of sidewalls in a reflecting SWTBLI. The wall-pressure measurements and oil flow visualization highlighted the resulting nonuniform surface flow pattern. The reverse flow regions spread laterally from the sidewall junctures on increasing shock strength, until they merged at the channel centerline. Bruce *et al.* [9] quantified the onset of three-dimensional behavior using the tunnel confinement ratio  $\delta^*/w$ , where  $\delta^*$  is the boundary-layer displacement thickness in the center of the tunnel and  $w$  is the tunnel width. They were able to vary the separation extent at the tunnel centerline by manipulating corner flows, hence establishing a link between the centerline and corner separation regions.

Burton and Babinsky [10] investigated this coupling for a Mach 1.5 normal SWTBLI in a rectangular channel. They observed that the compression waves generated at the corner smear the adverse pressure gradient imposed on the other parts of the flow field, leading to a smaller centerline separation. In a similar study carried out by Xiang and Babinsky [11], the influence of corner separation on the tunnel centerline was illustrated by estimating the position of the corner shock crossing point. This location was found by extrapolating the compression waves along a straight line. When the crossing point lies downstream of the interaction, the interaction is unaffected by the sidewalls and retains its quasi-two-dimensional nature. The main separation increases as the crossing point moves inside the interaction in the upstream direction. The separation extent decreases when the crossing point falls upstream.

Eagle and Driscoll [12] carried out detailed velocity and vorticity measurements using particle image velocimetry (PIV) in a rectangular channel flow at Mach 2.75. The surface streamline pattern on the sidewalls and the centerline region indicated certain similarities with type-1 and type-2 separation, respectively, as described by Tobak and Peake [19]. Morajkar *et al.* [20] analyzed a SWTBLI in a low-aspect-ratio duct using stereoscopic PIV measurements in a Mach 2.75 flow. The swept interactions on the sidewalls and the incident interaction on the bottom wall were coupled via a complex three-dimensional vortical flow field. Using the method of triple decomposition, three systems of vortices were identified: the corner vortex pair, swept-shock vortex on the sidewall, and a horseshoelike vortex associated with the bottom wall interaction. Funderburk and Narayanaswamy [13] performed experiments on a  $12^\circ$  compression corner at Mach 2.5. Both the primary and corner SWTBLI were investigated by surface streakline flow visualization and wall static pressure measurements. The pressure spectra in the intermittent region of the primary interaction were

broadband in nature with a peak at  $St = fL_{\text{sep}}/U_{\infty} \approx 0.01$ , consistent with the canonical two-dimensional version. On the other hand, the spectra corresponding to the intermittent region of the corner interaction was biased towards higher frequencies and displayed a peak at  $St \approx 0.05$ . Cross-coherence measurements indicated that pressure fluctuations in the incoming boundary layer drive the unsteadiness of corner SWTBLI, while the primary SWTBLI was more responsive to disturbances originating downstream.

Garnier [14] used stimulated detached-eddy simulations (SDES) to study the effect of sidewalls in a reflecting SWTBLI at Mach 2.3. The mean flow field reproduced all the essential flow features observed in the experiments. The corner flows were characterized by strongest level of fluctuations, but no statistical link was established with the flow at the centerline. Bisek [15] carried out high-fidelity simulations at Mach 2.25 on a  $24^\circ$  compression ramp with the presence of sidewalls. Both the centerline and sidewall shock fronts were characterized by low-frequency oscillations. On the other hand, the separation bubble did not exhibit similar behavior. Wang *et al.* [16] carried out large-eddy simulations (LES) of an oblique SWTBLI at Mach 2.7 for three different aspect ratios. They observed a swept interaction on the sidewalls, quasiconical in nature. The separation and reattachment translated upstream as the aspect ratio decreased. Meanwhile, the separation extent increased and stabilized to a length 30% higher than its corresponding quasi-two-dimensional counterpart.

Bermejo-Moreno *et al.* [21] carried out wall-modeled large-eddy simulations (WMLES) of a flow field characterized by multiple oblique SWTBLIs at Mach 2, in the presence of sidewalls. They considered three increasing strengths of the incident shock. The effect of confinement on the mean flow field resulted in the presence of a singular shock intersection in the first SWTBLI, as compared to a regular shock intersection in case of the spanwise-periodic simulation. Spectral analysis of wall-pressure fluctuations highlighted low-frequency content in the vicinity of the separation shocks. The low-frequency motions associated with different interactions in the flow field were coupled by a nonlinear mechanism. Lushner and Sandham [22] carried out a numerical investigation of a three-dimensional laminar shock-wave boundary-layer interaction (SBLI) at Mach 2. Critical point analysis close to the wall revealed streamline patterns that resembled an owl-face pattern of the first kind, as introduced by Perry and Hornung [23]. A swept conical SBLI present between the shock generator and sidewalls was responsible for the strengthening of the interaction downstream. Presence of high-speed streaks downstream of the interactions near the centerline and in the corner suggested streak instability as a possible transition mechanism in a confined SBLI.

Rabey *et al.* [17] investigated the off-centerline behavior in a reflecting SWTBLI with sidewall effects by analyzing results from LES and high-frequency pressure measurements from experiments. They observed asymmetry about the spanwise center with peak unsteadiness occurring off center. Using wall-pressure measurements, they were not able to find significant correlation between separations at the corner and center. Poggie and Porter [18] performed high-fidelity simulations of a  $24^\circ$  compression ramp at the same operating conditions used by Bisek [15]. The spanwise width of the domain was lower in this case in order to test the effect of a higher confinement ratio ( $\delta/w$ ). The curvilinear variation of the centerline separation extent with respect to the confinement ratio was verified. Using conditional averaging, the authors observed large-scale symmetric and asymmetric motion of the interaction.

This study is an extension of the analysis carried out by Poggie and Porter [18]. Based on the previous studies carried out on SWTBLI with sidewall effects, possible coupling between primary and corner separations as well as low-frequency unsteadiness can be expected to occur in the flow field. This study aims to verify the presence of these phenomena in this flow field. Additionally, frequency bands corresponding to various unsteady events are determined using spectral analysis. Statistical estimates of coherence and correlations are used to investigate the effect of the said events on the low-frequency unsteadiness. This paper is organized as follows: Section II outlines the computational setup used to obtain the results analyzed in this study, as well as presents the data analysis procedure. Section III A describes the features of the mean and instantaneous flow field. The organized structures present in the upstream boundary layer are also characterized. Wall-pressure

TABLE I. Free-stream conditions.

Parameter	Value
$U_\infty$	588 m/s
$M_\infty$	2.25
$\rho_\infty$	0.49 kg/m <sup>3</sup>
$T_\infty$	170 K
$T_w$	323 K
$\rho_\infty u_\infty / \mu_\infty$	$25 \times 10^6 \text{ m}^{-1}$
$\delta_o$	$6.096 \times 10^{-4} \text{ m}$

spectra for individual frequency components are illustrated in Sec. III B. The physical nature of the corresponding events is interpreted using results from previous studies. Sections III C and III D discuss the unsteadiness associated with the translational motion of the shock front and breathing motion of the separation bubble. The degree of influence of events determined from Sec. III A on both the phenomena is estimated by calculating the coherence magnitude. The coupling between centerline, corner, and sidewall separation regions is investigated using space-time correlations in Sec. III E. Finally, the conclusions of this study are presented in Sec. IV.

## II. METHODOLOGY

### A. Computational setup

The results of the simulations carried out by Poggie and Porter [18] are analyzed in this paper. The corresponding free-stream conditions are shown in Table I. The numerical calculations were performed by the higher-order plasma solver (HOPS) code. The compressible Navier-Stokes equations were solved under the assumption of thermally and calorically perfect gas. A second-order implicit Euler scheme was used for time integration with quasi-Newton subiterations. A sixth-order compact differencing scheme was used for spatial discretization of internal points, which was dropped to fifth and fourth order for points nearest to the boundaries. A Padé-type, nondispersive filter was used to ensure numerical stability. A shock capturing routine based on the approach of Visbal and Gaitonde [24] was implemented. For cells in the vicinity of the shock, a third-order upwind Roe scheme with a continuous limiter of Anderson *et al.* [25] was used. The spatial discretization switches back to the original compact scheme away from the shock. Additional details of the numerical schemes are presented in Refs. [18,26].

The computational mesh is shown in Fig 1. Its streamwise extent is  $X = x/\delta_o = 130$ , where  $\delta_o$  is the boundary-layer thickness at  $X = 80$ . The ramp begins at  $X = 100$  and is inclined at  $24^\circ$ . The spanwise width of the domain is  $Z = z/\delta_o = 20$ . The grid consisted of  $4711 \times 1420 \times 1401$  points in the  $x$ ,  $y$ , and  $z$  directions, respectively, totaling approximately to  $9.4 \times 10^9$  cells. The corresponding grid spacing in wall units is  $\Delta x^+ = 7.9$ ,  $\Delta y^+ = 0.51$ , and  $\Delta z^+ = 0.51$ . The grid was gradually stretched away from the floor and sidewalls towards the top boundary and center of the domain. At the inlet, a boundary-layer profile corresponding to the laminar-flow similarity solution for Mach 2.25 flow was imposed. The flow properties were extrapolated at the end and top of the domain.

Transition to turbulence was achieved by means of an artificial body force implemented on the floor (at  $X = 2.5$ ,  $Y = 0$ ) and sidewalls (at  $X = 2.5$ ,  $Z = 0, 20$ ). On the floor, the trip was uniform along the span and was set to zero close to the corners. The body force consisted of both streamwise and wall-normal components. It was oriented in the upstream direction, with a larger magnitude than the wall-normal component. The body force on the sidewalls was composed of streamwise and spanwise components, oriented in the upstream direction. The spanwise component was reversed

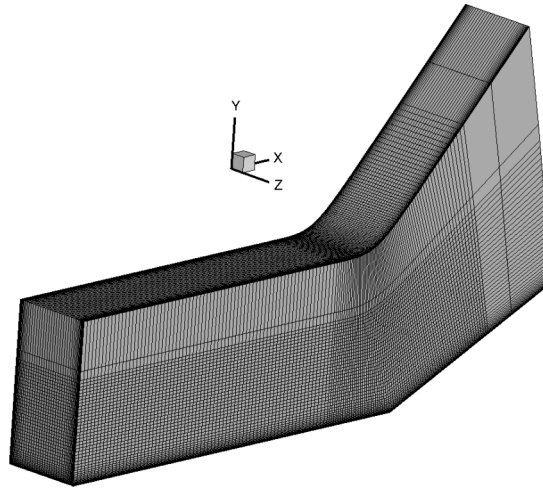


FIG. 1. Computational grid; every 32nd point shown for clarity.

on the sidewall at  $Z = 20$ . The mathematical expressions for implementation of the artificial trip model can be found in Ref. [18].

The calculations were run for  $2.39 \times 10^5$  iterations with a nondimensional time step of  $U_\infty t / \delta_0 = 5 \times 10^{-3}$ . This corresponds to an overall simulation time of  $U_\infty t / \delta_0 = 1195$ . The calculation was initially run for about two flow-through times to establish a statistically steady state. The flow data were then saved for about seven flow-through times. The data were extracted at six different planes (see Fig. 2): the three no-slip walls (planes 1–3), the  $X = 80$  plane (plane 4), the ramp-normal plane at  $X \approx 116$  (plane 5), and the portion of the center plane ( $Z = 10$ ) downstream of  $X = 80$  (plane 6). These planes were saved every 200 iterations which corresponds to a sampling frequency of  $f_s \approx 965$  kHz. The total duration of the data set corresponds to about 5.3 cycles of the low-frequency shock motion and breathing of the separation bubble ( $St \approx 0.03$ ) and about 50–60 cycles

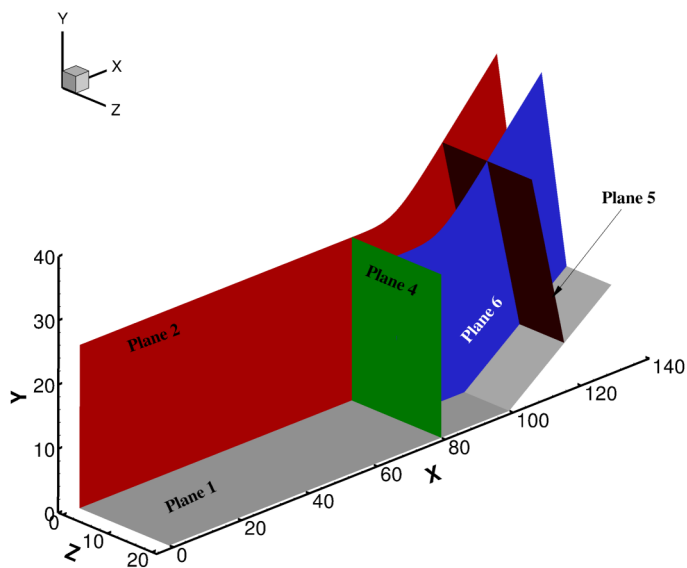


FIG. 2. Sampled planes (near surface omitted).

of the shear layer flapping and low-mid oscillations of the separation bubble ( $St \approx 0.1$ ) and Kelvin-Helmholtz vortex shedding ( $St \approx 0.5$ ). The authors acknowledge that the integration time limits the analysis of the low-frequency events, but assert that those in the mid-frequency range are time resolved.

### B. Data analysis

Data analysis was carried out by calculating the statistical estimates of correlation and coherence. The lengthscales and timescales in the flow field were determined via space-time correlations and two-point correlations. Their respective expressions are given in Eqs. (1) and (2), respectively:

$$R_{\alpha\beta}(x, y, \tau) = \frac{\overline{\alpha(x, y, t)\beta(x + r_x, y + r_y, t + \tau)}}{\sqrt{\sigma_\alpha^2 \sigma_\beta^2}}, \quad (1)$$

$$R_{\alpha\beta}(x, y) = \frac{\overline{\alpha(x, y, t)\beta(x + r_x, y + r_y, t)}}{\sqrt{\sigma_\alpha^2 \sigma_\beta^2}}, \quad (2)$$

where  $R_{\alpha\beta}$  is the correlation function between the two signals  $\alpha(t)$  and  $\beta(t)$ , with a displacement of  $r_x$  and  $r_y$  in the streamwise and wall-normal directions, respectively. The time delay is denoted by  $\tau$  and  $\sigma_\alpha^2$ ,  $\sigma_\beta^2$  represent the variance of  $\alpha(t)$  and  $\beta(t)$ . Spectral characteristics of turbulence were examined by calculating the power spectral density. The autospectral and cross-spectral densities were calculated using Eqs. (3a) and (3b) shown below [27]:

$$S_{\alpha\alpha}(f) = \int_{-\infty}^{\infty} R_{\alpha\alpha}(\tau) e^{-i2\pi f\tau} d\tau, \quad (3a)$$

$$S_{\alpha\beta}(f) = \int_{-\infty}^{\infty} R_{\alpha\beta}(\tau) e^{-i2\pi f\tau} d\tau. \quad (3b)$$

To determine the degree of linear correlation at a given frequency between the signals  $\alpha(t)$  and  $\beta(t)$ , the coherence magnitude ( $\gamma_{\alpha\beta}^2$ ) between the two was calculated using Eq. (4):

$$\gamma_{\alpha\beta}^2(f) = \frac{S_{\alpha\beta}(f)S_{\alpha\beta}^*(f)}{S_{\alpha\alpha}(f)S_{\beta\beta}(f)}, \quad (4)$$

where  $S_{\alpha\alpha}$  and  $S_{\beta\beta}$  are the autospectral densities of the signals  $\alpha(t)$  and  $\beta(t)$ , and  $S_{\alpha\beta}$ ,  $S_{\alpha\beta}^*$  are the respective cross-spectral densities, with the superscript ‘‘asterisk’’ denoting a complex conjugate. The process of segment averaging was used to calculate the statistical estimates in order to reduce the bias. The individual samples were extracted using a Hanning window to create an ensemble. The spectral density estimates were calculated using Welch’s method with 50% overlap between each segment. The segment lengths were long enough to resolve the lowest frequency  $f_l$  and were an integer multiple of  $2^k$ ,  $k \in \mathcal{I}$ , for efficient execution of the fast Fourier transform (FFT) algorithm. Based on the sampling frequency, the window segment size  $N_w = \max(f_s/f_l, 2^k)$ . The mean reattachment location was calculated by monitoring the sign of the streamwise component of skin-friction coefficient.

## III. RESULTS AND DISCUSSION

### A. Flow-field structure

In this section, the features of mean and instantaneous flow field are discussed. This is followed by a spectral analysis of wall-pressure fluctuations. Figure 3(a) shows the mean nondimensional wall pressure on the floor and left sidewall. The limiting streamlines (shown as black solid lines) and mean zero skin-friction contours ( $c_{f_x} = 0$ , shown as white solid lines) are included in the figure.

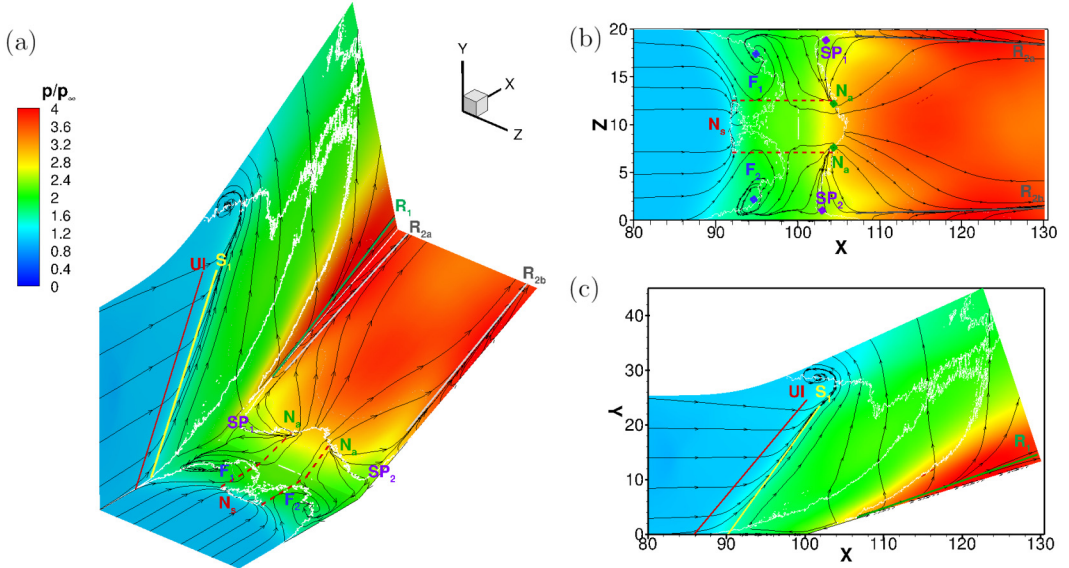


FIG. 3. Contours of mean wall pressure: (a) three-dimensional view, (b) projection on the ramp surface (plane 1), (c) projection on the left sidewall (plane 2). The ramp corner lies at  $X = 100$ .

The mean flow field on the floor shown in Fig. 3(b) is approximately symmetric about the spanwise center. The shock front, characterized by an abrupt pressure rise, is highly curved due to the influence of sidewalls. Based on the  $c_{fx} = 0$  contour, the flow separation at the corners occurs earlier than at the centerline. This occurs because the net momentum of the flow is lower due to the presence of two no-slip boundaries, making it more susceptible to the adverse pressure gradient imposed by the shock front. Across the span, the separation extent decreases away from the sidewalls, before increasing again close to the midspan. The compression waves generated due to sidewall separation regions modify the three-dimensional shock structure, thereby moderating the pressure gradient which lowers the separation extent.

Critical points deduced from the limiting streamlines are also highlighted in order to gain insight on the nature of separation and attachment of primary and corner flows. Shortly upstream of the separated zones between the midspan and sidewalls, the flow rolls up into two foci:  $F_1$  and  $F_2$ . Based on previous studies [9,11,12], these foci are expected to be the source of tornado vortices, lifting up fluid from the wall. The separation and reattachment in the vicinity of the centerline are characterized by a combination of nodes and saddle points [see Fig. 5(f) in Ref. [28]]. These regions are marked by red dashed lines and are indicative of two-dimensional separation and reattachment [28]. A separation node  $N_s$  and two attachment nodes  $N_a$  are included for clarity. Additionally, two saddle points  $SP_1$  and  $SP_2$  are present close to the left and right sidewall, respectively. Two reattachment lines  $R_{2a}$  and  $R_{2b}$  are a signature of corner vortices reattaching on to the ramp.

The mean flow features on the left sidewall in Fig. 3(c) are reminiscent of a swept SWTBLI caused by the compression ramp shock [29]. Surface flow features such as the upstream influence line  $UI$ , separation line  $S_1$ , and reattachment line  $R_1$  are noted in the figure. The incoming flow on the left sidewall begins to turn at  $UI$  and separates at  $S_1$ . The flow downstream of  $S_1$  is believed to turn into a separation vortex and follow a helical trajectory. As a result an open type of separation exists, wherein the flow does not recirculate upstream, as in a two-dimensional separation. Note that the separation extent grows downstream, as indicated by the  $c_{fx} = 0$  contour. The flow reattaches along the reattachment line  $R_1$ . This region is characterized by amplified aerothermal loads.

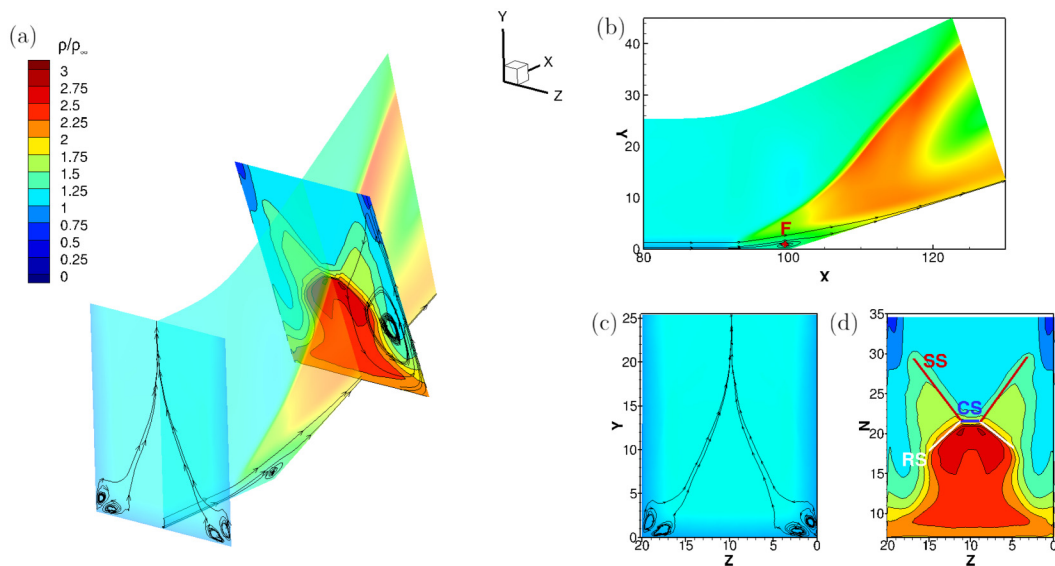


FIG. 4. Contours of mean density: (a) three-dimensional view, (b) projection on the streamwise plane at  $X = 80$  (plane 4), (c) projection on the ramp-normal plane (plane 5), (d) projection on the center plane at  $Z = 10$  (plane 6).

Figure 4 shows the mean density contours on the center plane ( $Z = 10$ ), streamwise plane at  $X = 80$ , and ramp-normal plane at  $X \approx 116$ . On the center plane in Fig. 4(b), a flow analogous to a classical two-dimensional interaction is present wherein the compression ramp shock splits into a  $\lambda$ -shock foot due to viscous effects. Within the separated zone, the focus point  $F$  suggests the presence of a horseshoe vortex. Combined with the results of the critical point analysis associated with Fig. 3, this interaction is judged to resemble an owl-face pattern of the second kind, as described by Perry and Chong [30] (see Fig. 22 in that reference). Although the centerline region resembles a quasi-two-dimensional SWTBLI, the flow does not recirculate upstream, but is swept away from the midspan by the horseshoe vortex originating at the focus point  $F$ . In Fig. 4(c), a pair of corner vortices are observed on the streamwise plane, upstream of the interaction. This feature was also present in the work of Bermejo-Moreno *et al.* [21], Wang *et al.* [16], Eagle and Driscoll [12], and Morajkar *et al.* [20].

On the ramp-normal plane in Fig. 4(d), specific features of the swept interaction described earlier can be visualized. Note that the direction normal to the ramp surface, labeled as  $N = n/\delta_o$ , is shown on the  $y$  axis. The compression ramp shock labeled as  $CS$  (shown as a solid blue line) bifurcates into  $\lambda$ -shock feet on both the sidewalls on account of the influence of sidewall boundary layers. The corresponding separation and reattachment shocks are labeled as  $SS$  and  $RS$ , respectively, as solid red and white lines. The streamlines close to the right sidewall highlight the separation vortex present downstream of the primary separation line  $S_1$  (see Fig. 3). This region extends from the foot of the separation shock and ends slightly above the ramp surface, downstream of the reattachment shock. As mentioned previously, the separation on the sidewalls is of the open type wherein the entrapped fluid follows a helical path downstream instead of recirculating upstream. Notice the drastically reduced spanwise extent of the compression ramp shock (highlighted using a solid red line) caused due to the growing separation extent on the sidewall. Following the outermost streamline over the separation vortex, the flow is compressed through the  $\lambda$ -shock foot. Downstream of the reattachment shock, it accelerates across the local expansion fan curving downwards and reattaching at  $R_1$  as an impinging jet. Such flows fall under the category of Edney type-IV interaction wherein the reattachment location is characterized by high aerothermal loads [31]. The vortex



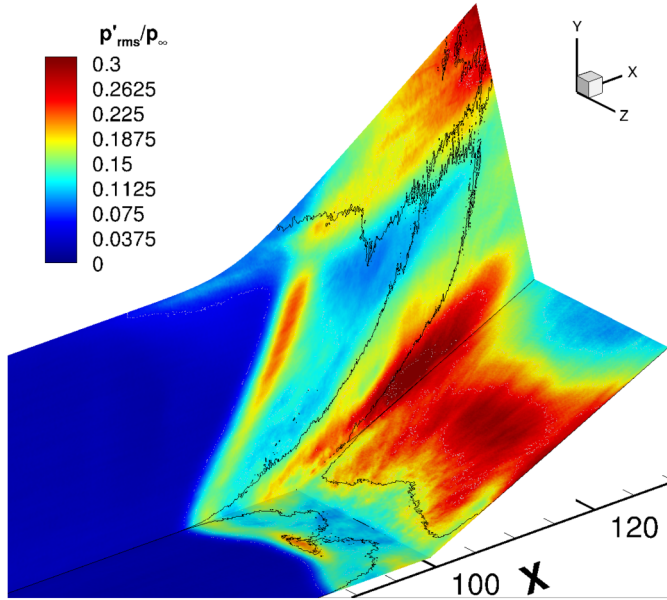


FIG. 5. Contours of RMS pressure. Black solid lines represent the  $c_{fx} = 0$  contour level.

system observed in this figure, a pair of corner vortices upstream of the interaction, a horseshoe vortex originating at the focus point  $F$ , and the swept sidewall vortices, is consistent with the results of Eagle and Driscoll [12] and Morajkar *et al.* [20].

The variation of Root Mean Square (RMS) of pressure fluctuations on the floor and left sidewall are shown in Fig. 5. The contour of  $c_{fx} = 0$  is shown as a black solid line on both the surfaces. The RMS pressure shows a steep rise across the shock front from its undisturbed value. The amplification of this quantity is higher across the primary interaction as compared to the corner interactions. This occurs most likely on account of reduced shock strength away from the centerline, which in turn is caused by the smearing effect of corner interactions mentioned previously. Within the separated zone on the floor, the RMS pressure fluctuations decrease in magnitude before increasing dramatically downstream of reattachment on the ramp. The peak value occurs approximately at  $X = 117$ . Farther downstream, the fluctuations gradually decrease and approach the undisturbed level towards the end of the domain. A similar pattern is observed on the left sidewall, with peak values lying along the reattachment line  $R_1$  (see Fig. 3).

Figure 6 shows the instantaneous snapshot of the flow field. In order to exclude the right sidewall for visualization purposes, the domain is truncated at  $Z = 16$ . Contours of density gradient magnitude ( $|\nabla\rho|$ ) on four  $y$ - $z$  planes highlight the evolution of the shock structure along the streamwise direction. Additionally, contour lines of the same quantity are shown on the center plane ( $Z = 0$ ) to visualize the centerline shock structure. The isosurfaces of zero streamwise velocity ( $u/U_\infty = 0$ ), colored by nondimensional pressure ( $p/p_\infty$ ), distinguish the separated regions on the left sidewall and the floor.

The contour plot of  $|\nabla\rho|$  on the streamwise plane at  $X \approx 95$  is shown in Fig. 6(b). The contours consist of a distinct compression ramp shock, spanning almost the entire domain width. Close to both the sidewalls, the viscous effects cause it to bifurcate into a  $\lambda$ -shock structure. On the planes lying at  $X \approx 103$  and  $X \approx 110$  in Figs. 6(c) and 6(d), respectively, the spanwise extent of the compression ramp shock gradually decreases on account of increasing separation extent on the sidewalls. This phenomenon also pushes the  $\lambda$ -shock structures closer to each other and towards the center of the domain. The strength of the reattachment shock, within the  $\lambda$ -shock foot, is higher than the separation shock, which is smeared closer to the left sidewall. Also notice the slip surfaces

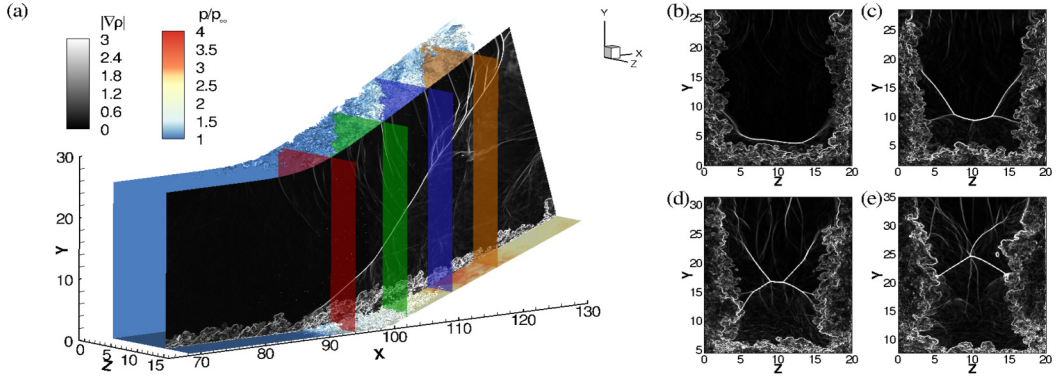


FIG. 6. (a) Instantaneous flow field. Isosurfaces of  $u = 0$  are colored with the magnitude of nondimensional pressure. Contours of density gradient magnitude are shown on the center plane ( $Z = 0$ ) and colored streamwise planes at (b)  $X = 95$  (red), (c)  $X = 103$  (green), (d)  $X = 110$  (blue), and (e)  $X = 117$  (orange).

emanating from the triple points. At  $X \approx 117$  in Fig. 6(e), the two  $\lambda$ -shock structures intersect, leading to reflected shock waves downstream. This event is most likely responsible for the regions of high RMS pressure values on the floor in the range  $110 \lesssim X \lesssim 120$ , downstream of reattachment (see Fig. 5).

The isosurfaces of  $u/U_\infty = 0$  indicate earlier separation at the sidewalls, consistent with the mean flow field shown in Fig. 3. On the center plane, the shock structure resembles to that of a quasi-two-dimensional interaction. The separation shock is distinct and higher in strength as compared to the reattachment shock, which is relatively smeared. Compression waves emanating from the eddies within the separated shear layer as well as the redeveloping boundary layer coalesce to form shocklets. The compression ramp shock seems to split into multiple shock waves downstream of the intersection location of sidewall  $\lambda$ -shock structures ( $X \gtrsim 110$ ) and towards the top boundary. Regions lying above the compression ramp shock are populated by waves resulting from reflection at the top boundary.

The downstream evolution of the shock structure is shown in Fig. 7 using contours of density gradient magnitude. The contours are plotted on four  $x$ - $z$  planes at different wall-normal coordinates as shown Fig. 7(a), with the respective top views presented in Figs. 7(b)–7(e). At the lowermost wall-normal location in Fig. 7(b), the compression ramp shock spans a major portion of the

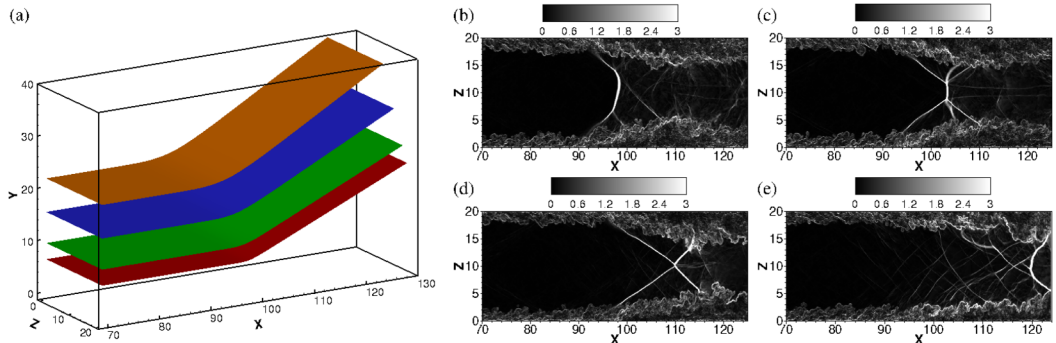


FIG. 7. Contours of instantaneous density gradient magnitude ( $|\nabla\rho|$ ) on inclined planes (at constant  $j$  values). (a) Location of extracted planes in the domain (b)  $j = 620$  (red), (c)  $j = 750$  (green), (d)  $j = 1000$  (blue), (e)  $j = 1270$  (orange).

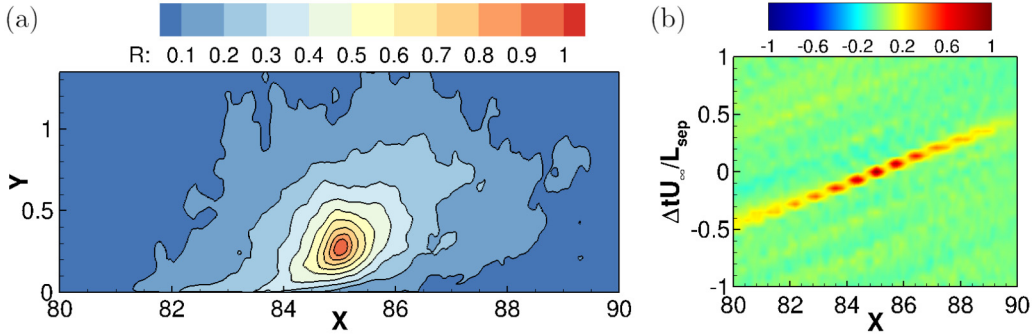


FIG. 8. (a) Two-point correlations. (b) Space-time correlations of streamwise velocity fluctuations.

domain width. Viscous effects at the sidewalls lead to bifurcation of the shock into a  $\lambda$ -shock foot. Notice the bending of the compression ramp shock caused by sidewall effects. Wang *et al.* [16] and Bermejo-Moreno *et al.* [21] also observed a similar bending of the incident shock in their study of a reflecting SWTBLI with sidewalls. The latter attributed this to the presence of corner shocks and strong lateral motions. Flow separation on the sidewalls caused by the imposed adverse pressure gradient is also evident from the figure. A complex wave pattern, mostly composed of compression waves emanating from the eddies in the boundary layer, is present downstream of the shock.

Figure 7(c) shows the shock structure on the plane  $j = 750$ . At this height, the spanwise extent of the compression ramp shock is reduced significantly, while strength of the  $\lambda$ -shock feet is higher. There are two sets of slip lines originating from the triple points. One is oriented towards the floor (see the plane at  $X \approx 102$  in Fig. 6), and the other is aligned with the core flow. At  $j = 1000$  in Fig. 7(d), the  $\lambda$ -shock structures on the sidewall are on the verge of intersection. The resulting wave structure towards the domain exit [shown in Fig. 7(e)] resembles a bow shock, with a clutter of compression waves lying immediately upstream.

Figure 8 describes the lengthscale and timescale of large-scale structures present in the upstream boundary layer. Two-point and space-time correlations of streamwise velocity fluctuations are used for this purpose. Superstructures in the logarithmic region of a turbulent boundary layer were observed in the experiments carried out by Ganapathisubramani *et al.* [32,33], who later showed that the timescales involved matched closely with that of the low-frequency shock oscillations. Beresh *et al.* [34], Porter and Poggie [35], and Pirozzoli and Grasso [36] arrived at similar conclusions. For the two-point correlations, the reference signal was extracted at  $(X, Y) \approx (85.02, 0.28)$ , which was correlated with streamwise velocity fluctuations within the boundary layer and upstream of the interaction.

The contours in Fig. 8(a) are elliptical in shape whose major axes are inclined with respect to the streamwise direction. This angle increases for contours associated with higher correlation magnitude. The nature of the contour plot agrees with the results of experiments of Ganapathisubramani *et al.* [32,33]. Based on the  $R = 0.5$  contour level, the streamwise length scale is  $l_x \approx 1.29\delta_0$ . Space-time correlations of the same quantity were used to deduce the convection velocity of these structures. The reference point was same as the previous case, and the signal corresponding to that location was correlated with similar signals along the streamwise direction, while maintaining the wall-normal coordinate. The resulting plot is shown in Fig. 8(b). Time delay scaled by the separation extent at the centerline ( $L_{sep}$ ) and free-stream velocity ( $U_\infty$ ) is plotted on the y axis with the streamwise coordinates on the x axis. The contour plot exhibits regions of high correlation magnitude along a straight line. The corresponding slope leads to a nondimensional convection velocity of  $U_c/U_\infty = 0.78$ .

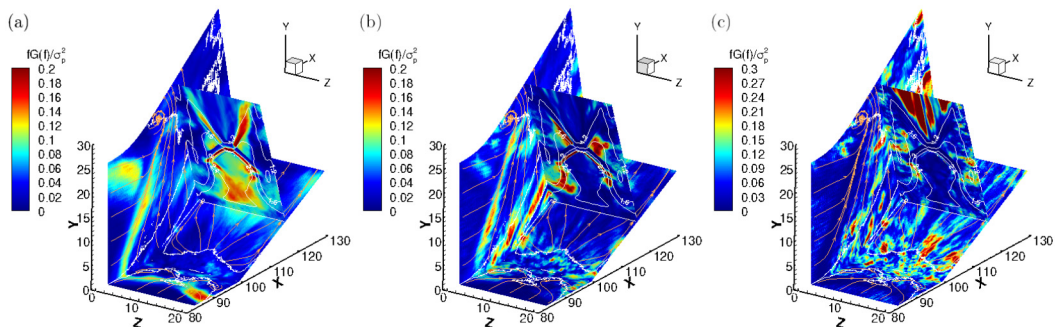


FIG. 9. Premultiplied pressure spectra on the floor, left sidewall, and ramp-normal plane (a)  $St = 0.03$ , (b)  $St = 0.12$ , (c)  $St = 0.54$ . The  $c_{fx} = 0$  contour is shown as a white solid line. Limiting streamlines in orange are included for reference. Mean density contours are shown on the ramp-normal plane.

### B. Unsteadiness of the flow field

This section presents a map of unsteadiness in the flow field by plotting wall-pressure spectra for individual frequency components. Based on previous studies [5,6,36,37], a SWTBLI is characterized by mid-frequency motion of the bubble ( $St \approx 0.1$ ) and high-frequency Kelvin-Helmholtz shedding ( $St \approx 0.5$ ), in addition to low-frequency shock motion and bubble breathing ( $St \approx 0.03$ ). Grilli *et al.* [38] used DMD to analyze the unsteady modes in a SWTBLI. Using the first four dominant modes occurring at low frequency, they were able to reproduce the pulsating motion of the separation bubble and low-frequency streamwise oscillations of the shock. Presence of similar events in this flow field was investigated by examining the wall-pressure spectra. The spectra were calculated using Welch's method with 50% overlap between each segment. Based on the net simulation time mentioned in Sec. II, a total 908 samples of data at select planes in the domain were available. To estimate the power spectral density, an ensemble of two signals with 454 samples each was created. An additional sample obtained from the overlap process was used for averaging, in conjunction with the original two samples.

The contours of premultiplied spectral energy are plotted initially on the floor (plane 1), left sidewall (plane 2), and ramp-normal plane (plane 5), followed by the center plane (plane 6). In the following figures,  $fG(f)/\sigma_p^2$  is the premultiplied spectral energy,  $f$  is the frequency,  $G(f)$  is the power spectral density, and  $\sigma_p^2$  is the variance. Based on the window segment size, a frequency resolution of  $\Delta St = \Delta f L_{sep}/U_\infty \approx 0.03$  was obtained. The contours are plotted for  $St_1 = 0.03$ ,  $St_4 = 0.12$ , and  $St_{18} = 0.54$ , where  $St_k = f_k L_{sep}/U_\infty = k f_s L_{sep}/N_w U_\infty$ . The results for the first case are shown in Fig. 9. The domain size was reduced by calculating the spectra at every 10th point in the streamwise direction and every 5th point in the wall-normal and spanwise directions, respectively. Limiting streamlines, as well as the  $c_{fx} = 0$  contours are superimposed on the floor and left sidewall. Contours of mean density are shown on the ramp-normal plane.

We start from the lowest-frequency component in Fig. 9(a). The spectral energy on the floor is higher along a narrow band present at the separation line. As we are dealing with the frequency component typically associated with shock oscillations, this region most likely corresponds to its intermittent length. Similar regions were also observed by Rabey *et al.* [17] for the case of a reflecting SWTBLI. The contours are asymmetric across the centerline, with higher-energy magnitude close to the right sidewall. We expect that such asymmetry would disappear with averaging over long simulated times. The streamwise extent of this band varies along the span. It is higher close to the sidewalls and decreases progressively towards the centerline. This observation agrees with the results of Rabey *et al.* [17] which suggest a stronger prevalence of low-frequency content close to the sidewalls for cases with smaller aspect ratios. It is possible that the compression waves generated

by the corner separations are locked in with the oscillations of the shock front, thereby resulting in larger regions with dominant low-frequency content.

Moderate magnitudes of spectral energy are observed in a localized region on the ramp ( $110 \leq X \leq 125$ ), downstream of reattachment. This region is also characterized by high values of RMS pressure (see Fig. 5), which were a result of reflection of the  $\lambda$ -shock feet on the sidewalls. Hence, the moderate to high values of spectral energy can be attributed to the low-frequency oscillations of the shock system post reflection. On the left sidewall, the intermittent length of the swept shock oscillations in the vicinity of the separation line  $S_1$  is distinguished by high magnitudes of energy. The peak value occurs away from the wall at  $Y \approx 15$  and decreases dramatically at higher wall-normal coordinates. Farther downstream on the left sidewall, the presence of lower magnitudes suggests that events at higher frequencies occur in these regions.

In the ramp-normal plane,  $\lambda$ -shock feet on both the sidewalls are composed of regions with high-energy magnitudes. This observation suggests coherent streamwise oscillations of the entire shock system in the domain. Additionally, moderate magnitudes of energy are also present in the region between the  $\lambda$ -shock feet. This may be a result of a local compression wave system locked in with the oscillations of the shock system. Within the core flow region, the spectral energies increase progressively as the ramp surface is approached. This region consists of several gas-dynamic features present in an Edney type-IV interaction, namely, slip surfaces, expansion fans, and impinging jets, and seem to possess similar unsteady characteristics.

Figure 9(b) illustrates the contours of premultiplied energy density associated with the mid-frequency component:  $St = 0.12$ . On the floor, features such as the narrow band of high spectral energy in the vicinity of separation, as well as a similar localized region present downstream of reattachment on the ramp surface, are no longer visible. Instead, both the sidewall junctures are interspersed with relatively smaller regions characterized by events of this timescale. Based on their location, it is possible that these events are associated with the corner vortices. On the left sidewall, high magnitudes of spectral energy tracing the intermittent length of the  $\lambda$ -shock foot suggest a mid-frequency component, in addition to a low-frequency component.

Additionally, regions in the vicinity of the  $c_{f_x} = 0$  contour as well as along the reattachment line  $R_1$  are characterized by events at mid frequencies. Physically these events may be representative of the vortex rollup process, flapping of the separated shear layer in the vicinity of separation, and unsteadiness of the impinging jet at  $R_1$ . On the ramp-normal plane, regions close to the triple points are highlighted by high magnitudes of spectral energy. These regions include the  $\lambda$ -shock feet as well as the compression fan system between their legs. Presence of high-energy magnitudes over the separation vortex may be indicative of unsteadiness associated with the expansion fan, which typically occurs in the Edney type-IV interaction.

The contours of premultiplied energy density for a high-frequency component ( $St_{18} = 0.54$ ) are shown in Fig. 9(c). Notice that the bands of high-energy magnitudes characterizing shock oscillations on both the floor and left sidewall are no longer present in this case. Instead, regions within the separated zone (delineated by the  $c_{f_x} = 0$  contour) are representative of events at this frequency. These zones most likely correspond to the unsteadiness associated with small-scale turbulence. Also, bands of high magnitude of spectral energy are observed at locations in the vicinity of centerline reattachment. Based on the frequency component in consideration, these bands are most likely associated with vortex shedding from the separated shear layer. A similar trend is observed on the left sidewall. On the ramp-normal plane, the  $\lambda$ -shock feet are no longer distinguished by high-energy magnitudes. Following the pattern on the floor and left sidewall, such regions now occur within the separation vortex.

Figure 10 illustrates the premultiplied pressure spectra for individual frequency components (used in Fig. 9) on the center plane. Spectral estimates were calculated by adapting the same procedure employed to determine the wall-pressure spectra in Fig. 9, with the same frequency resolution. The black solid and dashed lines represent the mean dividing streamline ( $u/U_\infty = 0$ ) and the sonic line, respectively. The dashed-dotted line in Fig. 10(c) highlights the incoming boundary layer. Starting from the lowermost frequency component ( $St = 0.03$ ) in Fig. 10(a), the entire extent

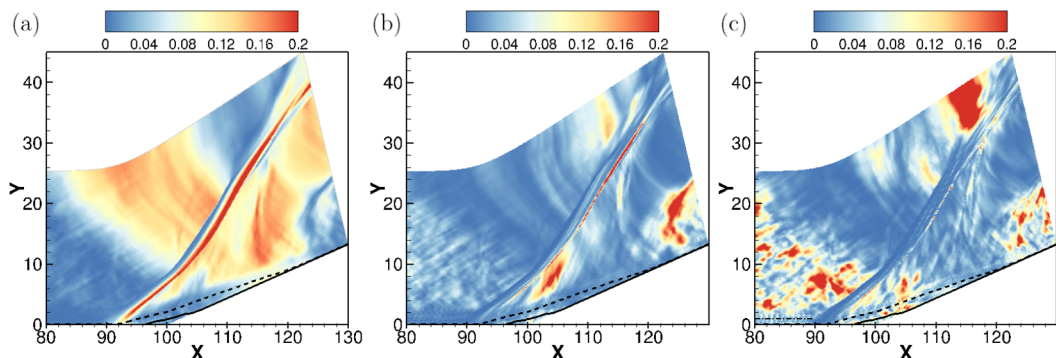


FIG. 10. Contours of pre-multiplied pressure spectra  $[fG(f)/\sigma_p^2]$  on the center plane ( $Z = 0$ ): (a)  $St = 0.03$ , (b)  $St = 0.12$ , (c)  $St = 0.54$ . Solid and dashed black lines indicate the mean dividing streamline ( $u/U_\infty = 0$ ) and the sonic line, respectively. The dashed-dotted line in part (c) highlights the boundary-layer edge upstream of the interaction.

of the compression ramp shock is characterized by high magnitudes of spectral energy, signifying its low-frequency streamwise oscillations. This region ends approximately at the sonic line. The spectral magnitude drops significantly within the centerline separation region. Regions of moderate energy magnitudes are also present above and below the compression ramp shock. Such regions may be caused by oscillations of certain features of the sidewall interaction, i.e., local compression waves above the shock and expansion fans, slip surfaces below the shock (see Figs. 6 and 7). Post reattachment, the spectral energy magnitude increases approximately in the range  $116 \leq X \leq 120$ . This observation, consistent with the results in Fig. 9(a), can be attributed to the reflection of sidewall  $\lambda$ -shock feet.

In case of the second frequency component ( $St = 0.12$ ), the contours of pre-multiplied spectral density shown in Fig. 10(b) exhibit a significantly lower-energy magnitude along the trace of the reflected shock foot. Farther away from the floor, high-energy magnitudes persist along the remainder of the shock. Hence, it seems that motion of the reflected shock foot is dominated by the low-frequency component, while motion of the shock away from the wall is characterized by both low-frequency and low mid-frequency components. The sidewall shock system follows a similar trend [see Fig. 9(b)]. Contours of pre-multiplied energy density for the final frequency component ( $St = 0.54$ ) are shown in Fig. 10(c). In this case, the region within the centerline separation consists of events associated with this timescale. The compression ramp shock is no longer highlighted by high-energy magnitudes. Moderate magnitudes of energy are observed upstream of the interaction, aligned approximately along the Mach lines emanating from the incoming boundary layer. In both the figures, the region of high-energy density is present approximately in the top-right corner of the center plane may be related to the presence of the sponge layer (not included in the figure), and is physically not relevant for this analysis.

### C. Unsteadiness of the shock front

This section discusses the spectral characteristics of oscillations of the compression ramp shock and the  $\lambda$ -shock feet on the sidewalls. Henceforth, these two features will be collectively referred to as the “shock front.” The time histories of shock location are extracted at the centerline and the juncture at the left sidewall. A pressure-based threshold method devised by Porter and Poggie [35] was used for this purpose. At every time step, the instantaneous pressure ( $\tilde{p}$ ) at the desired location was monitored. The shock location at a particular instant was assigned the streamwise value at which  $\tilde{p} \geq p_\infty + 10\sigma_p$ , where  $p_\infty$  is the free-stream pressure and  $\sigma_p$  is the RMS of pressure fluctuations in an undisturbed boundary layer.

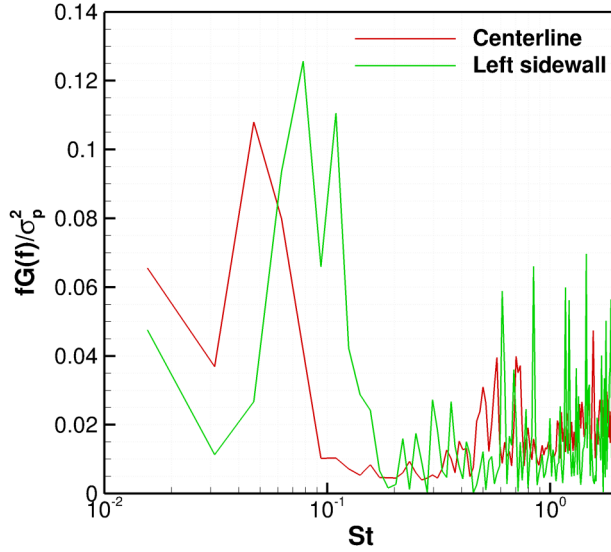


FIG. 11. Spectra of shock oscillations.

The spectral estimates were calculated using Welch's method. In order to resolve frequencies lower than  $St = 0.03$ , no windowing was carried out, i.e., the segment size was  $N_w = 908$ . The corresponding lowermost frequency component is  $St_1 = f_s L_{sep} / N_w U_\infty \approx 0.015$ . In the case of the centerline shock history, to compensate for the lack of ensemble averaging, the spectra were instead averaged across the span in order to improve the signal-to-noise ratio. Based on the critical point analysis in Fig. 3(b), the centerline interaction shows quasi-two-dimensional behavior for  $7.23 \lesssim Z \lesssim 12.63$  (marked by red dashed lines in the figure). The aforementioned spanwise averaging was carried out within this domain. In case of the left juncture, spanwise averaging was not possible as that region is characterized by strong three-dimensional effects. The resulting shock spectra are shown in Fig. 11.

The spectra are shown in pre-multiplied coordinates, with Strouhal number on the  $x$  axis. In case of the centerline shock, a distinct peak is present  $St \approx 0.04$ , consistent with the observations in spectra shown in Fig. 9(a). A spectral plot characterizing shock motion at the left juncture shows a peak at a slightly higher frequency ( $St \approx 0.08$ ), but is of the same order of magnitude. A second peak of almost similar magnitude occurs at  $St \approx 0.11$ , which might be caused by the presence of corner vortices or could be a statistical artifact. A similar trend was observed in the experiments of Funderburk and Narayanaswamy [13], who obtained a higher peak Strouhal number for the corner interaction  $St_L \approx 0.05$  as compared to the primary interaction  $St_L \approx 0.01$ , where  $St_L = f L_{sep} / U_\infty$ . The spectrum for the centerline shock oscillations is slightly smoother at higher frequencies on account of spanwise averaging. Using these respective time histories, the causes and effects of shock unsteadiness on the entire domain were investigated by calculating the coherence magnitude [see Eq. (4)] with pressure fluctuations.

The template used to present the results in Sec. III B is reproduced here, wherein contours of coherence magnitude are shown for individual frequency components. The coherence magnitude was estimated by averaging over an ensemble of two segments, each consisting of 454 samples, resulting in a frequency resolution of  $\Delta St = 0.03$ . Figure 12 displays the contours of coherence on the floor, left sidewall, and ramp-normal plane, as well as on the center plane. The time history of centerline shock oscillations was used as the reference signal. Limiting streamlines on the floor and left sidewall are illustrated using solid black lines. On the center plane, the black solid and dashed lines represent the mean dividing streamline ( $u/U_\infty = 0$ ) and the sonic line, respectively; the

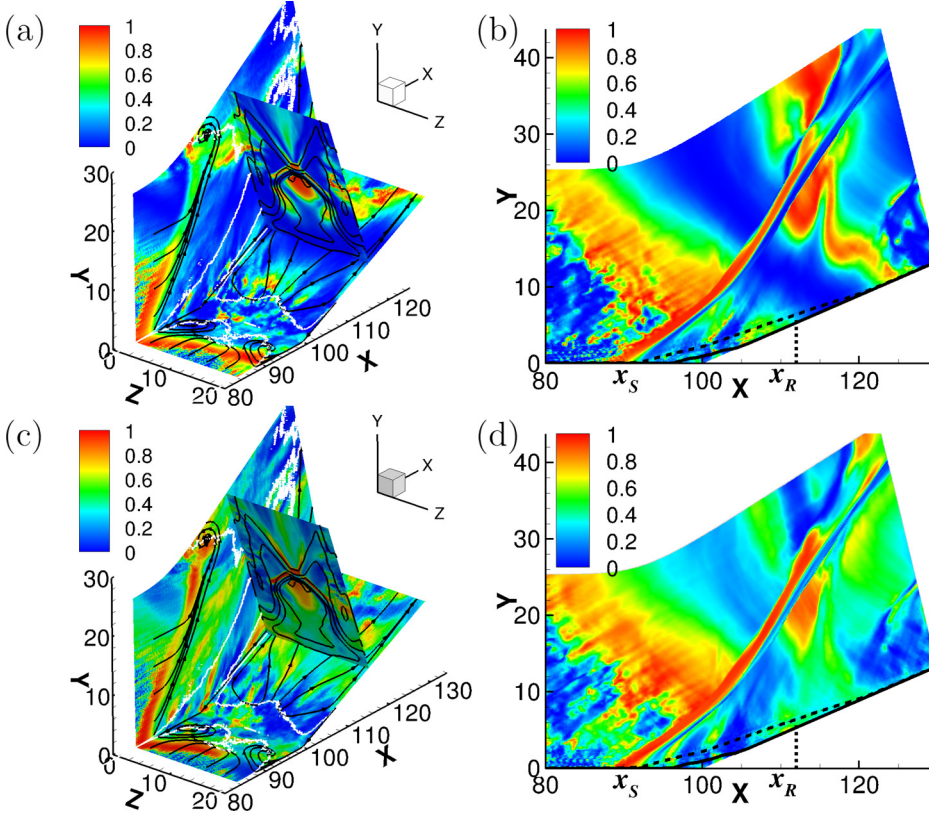


FIG. 12. Coherence of centerline shock oscillations with pressure fluctuations for frequency component: (a), (b)  $St = 0.03$ , (c), (d)  $St = 0.06$ . In (a) and (c), the solid black and white lines on the floor and left sidewall represent the limiting streamlines and  $c_{f_x} = 0$  contour, respectively. Solid black lines on the ramp-normal plane indicate the mean density contours. Solid and dashed black lines on the center plane in (b) and (d) indicate the mean dividing streamline ( $u/U_\infty = 0$ ) and the sonic line, respectively.

mean separation ( $x_S \approx 92$ ) and reattachment locations ( $x_R \approx 112$ ) are also highlighted for reference. Contours of mean density (see Fig. 4) are shown on the ramp-normal plane. The corresponding contour labels are not included to reduce clutter. Since the low-frequency unsteadiness associated with shock oscillations is of primary interest, the coherence plots corresponding only to the first two frequency components, i.e.,  $St_1 = 0.03$  and  $St_2 = 0.06$ , are discussed. The coherence plots can be interpreted as follows: the red region represents high values of coherence (strong linear relationship), the yellow-green region represents moderate values of coherence (weakly linear relationship), and the blue region is comprised of low coherence magnitudes (weak or nonlinear relationship).

In case of the lowermost frequency component shown in Fig. 12(a), a band of high coherence magnitude on the floor, lying approximately at  $X = 90$ , is indicative of the pressure fluctuations induced by the low-frequency shock motion. This band is slightly skewed in the upstream direction towards the left sidewall. Small patches of moderate to high coherence are observed within the centerline separation, suggesting an overall weakly linear relationship of shock motion with the corresponding events. Similar regions are present downstream of reattachment. It is possible that they are associated with the unsteadiness of the centerline separation bubble, which in turn affect the shock motion via a feedback mechanism.

On the left sidewall, high to moderate coherence magnitudes present along the primary separation line are caused by the oscillations of  $\lambda$ -shock feet, which are coupled with those of the centerline



shock. Any events downstream of the primary separation line seem to be uncorrelated with the centerline shock motion. On the ramp-normal plane, moderate coherence magnitudes are observed shortly downstream of the separation shock foot (of the  $\lambda$ -shock structure), which persist only for a short distance. The portion of the separation shock foot closer to the sidewalls is characterized by low coherence magnitudes. This suggests that the concomitant oscillations are not strongly coupled with the centerline shock motion, and may be caused by a different phenomenon. Regions close to the triple points consisting of slip surfaces, as well as on the upper boundary of the separation vortex, are well correlated with the centerline shock motion.

On the center plane in Fig. 12(b), nearly the entire trace of the compression ramp shock is highlighted by high coherence magnitude. It decreases to low values towards the top-right corner of the domain. Additionally, high values of coherence below the compression ramp shock ( $x_R \lesssim X \lesssim 125$ ) may be indicative of low-frequency oscillations of the shock front formed due to interaction between the sidewall  $\lambda$ -shock feet (see Fig. 6). Moderate values of coherence are present in the vicinity of the mean reattachment location, which is consistent with the results of Thomas *et al.* [39], Priebe and Martín [40], and Agostini *et al.* [37].

Figure 12(c) shows the trend of coherence for the frequency component  $St = 0.06$ . On the floor, the previously observed band of high coherence does not extend across the entire span. Instead, it begins from the left juncture and ends at  $Z \approx 16$ . Akin to the previous case, this region is skewed in the upstream direction towards the left sidewall, though the skew angle is comparatively higher. The coherence decreases to moderate magnitudes towards the right sidewall. Based on the limiting streamlines, the events at the foci  $F_1$  and  $F_2$  display a weakly linear relationship with the shock motion. Increased coherence magnitudes are also observed for events within the separated zone and downstream of reattachment.

On the left sidewall, coherence increases along the primary separation line as well as downstream of this location. A similar pattern is noted on the ramp-normal plane, with the exception that the motion of  $\lambda$ -shock feet are not well correlated with the centerline shock oscillations at this particular frequency. The coherence contours on the center plane for this frequency component follow a similar pattern as that in the case of  $St = 0.03$ . A similar exercise was carried out with the left sidewall shock location history as the reference signal (not shown here for brevity). The coherence contours for the lowermost frequency components ( $St = 0.03$  and  $0.06$ ) mostly followed the trend present in Fig. 12. Some notable differences were manifested as increased coherence magnitudes as well as a higher skew angle of the band of high coherence on the floor. Additionally, the coherence plots indicated that the left sidewall shock oscillations were in phase with those of the centerline shock.

Based on these results, we make some inferences regarding the nature of oscillations of the shock front. Figure 12 highlighted a band of high coherence on the floor, skewed in the upstream direction at the left sidewall. This observation suggests that the portion of the shock front lying on the left of the center plane ( $Z = 10$ ) translates upstream. This upstream movement may be caused by the expansion of the sidewall separation region. Similar phenomenon can be expected to occur at the right sidewall, resulting in the alternate back and forth movement of the interaction. Poggie and Porter [18] used conditional averaging to observe similar large-scale asymmetric motion. In case of the lowermost frequency component ( $St = 0.03$ ), the coherence magnitude along the separation shock foot (within the  $\lambda$ -shock structure) suggests a nonlinear coupling with the centerline shock oscillations. On the other hand, the motion of the reattachment shock foot and slip surfaces is locked in with the centerline shock motion.

Figure 13 shows the space-time correlations of streamwise velocity fluctuations upstream of the interaction, with the centerline shock oscillations. The correlation estimates were calculated by averaging over an ensemble of two signals with 454 samples each. The signals are extracted along the wall-normal direction at  $X \approx 85.02$ . The contour plot in this figure shows variation of the correlation magnitude along the wall-normal direction, corresponding to various values of nondimensional time delay. The edge of the boundary layer lies at  $Y \approx 1.1$ . In this figure, localized regions of high correlation magnitude are observed both within and outside the boundary-layer edge. They occur at positive values time delay, which lie in the range  $20 \leq \Delta t L_{sep}/U_\infty \leq 30$ .

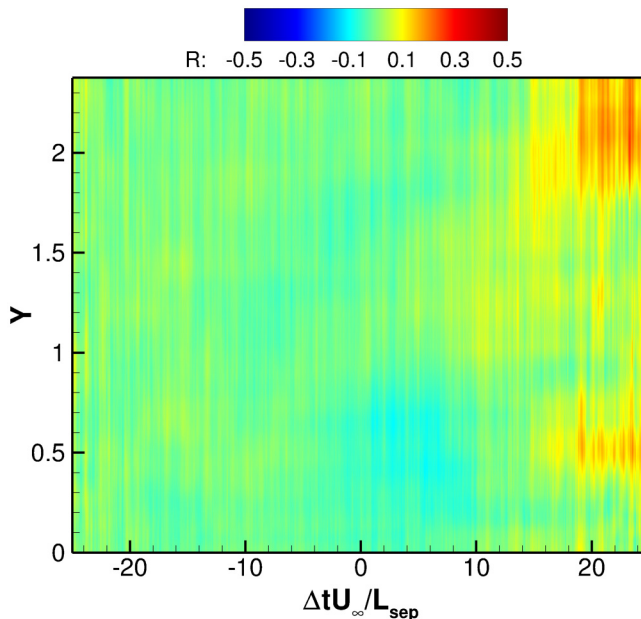


FIG. 13. Upstream influence of large-scale structures on separation shock motion.

Therefore, any event occurs first in the upstream boundary layer, which then affects the shock motion. Additionally, positive correlations suggest that a downstream movement of the shock foot ( $x'_{shk} > 0$ ) is associated with a higher net momentum in the upstream boundary layer ( $u' > 0$ ), and vice versa. This observation is consistent with the results of Ganapathisubramani *et al.* [32], Beresh *et al.* [34], and Porter and Poggie [35]. The Strouhal numbers corresponding to the optimal values of time delay ( $St = 1/T$ ) lie approximately in the range  $0.03 \leq St \leq 0.05$ , which includes the dominant frequency of centerline shock oscillation (see Fig. 11). Localized region of high correlation magnitude outside the boundary-layer edge may be representative of Mach waves locked in with the shock oscillations.

#### D. Unsteadiness of the centerline separation bubble

In this section, we focus only on the centerline separation. The unsteadiness of separation bubble breathing is characterized in terms of its spectral content. Coherence magnitudes are used to determine the relationship with other events in the domain, which is analogous to the approach used in Sec. III C. We begin by estimating the spectra of separation bubble breathing. For this purpose, the mass history of the bubble was extracted using Eq. (5):

$$m(t) = \iiint_{\mathcal{V}} \rho(\mathbf{x}, t) f(\mathbf{x}, t) dx dy dz. \quad (5)$$

In the above equation,  $\rho(\mathbf{x}, t)$  is the instantaneous density. Note that on the center plane ( $Z = 10$ ), the  $dz$  term drops out, thereby transforming the volume integral to a surface integral. Separation bubbles in quasi-two-dimensional interactions are characterized by upstream flowing fluid. At any specific instant, regions of both upstream and downstream fluid are present within the bubble. Therefore, to exclude the regions of downstream flow, a simple switch function  $f(\mathbf{x}, t)$  was incorporated in Eq. (5). The mathematical expression for this switch function is shown in Eq. (6):

$$f(\mathbf{x}, t) = \begin{cases} 1, & u(\mathbf{x}, t) < 0 \\ 0, & u(\mathbf{x}, t) \geq 0. \end{cases} \quad (6)$$

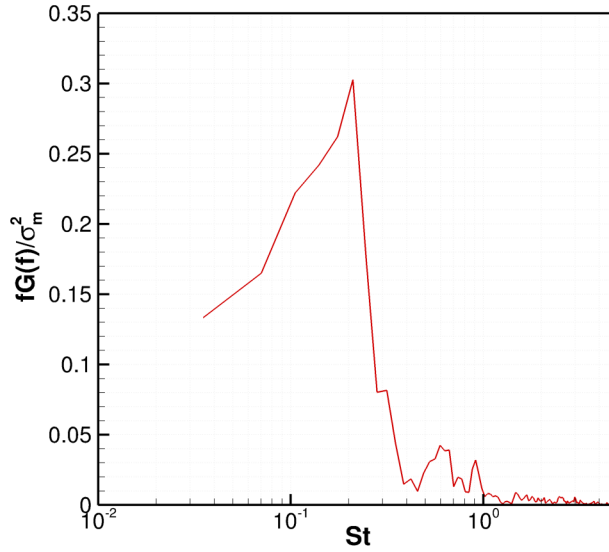


FIG. 14. Spectra of centerline separation bubble unsteadiness.

The numerical integration was carried out using the trapezoidal rule at every instant in time. Once the mass history was obtained, the spectra were calculated using Welch's method without segment averaging in order to resolve the lower frequencies. The resulting spectrum is shown in Fig. 14. The premultiplied spectral density is plotted on the vertical axis and the Strouhal number is shown on the horizontal axis in a logarithmic scale. The spectrum displays a peak at  $St \approx 0.11$ , with significant energy present in the lower frequencies. Previous studies on SWTBLI highlighted both the low-frequency breathing mode as well as the mid-frequency mode [41,42]. The latter is typically the response of the separation bubble to shear-layer flapping or shedding of vortical structures.

The influence of separation bubble unsteadiness on the domain is examined by calculating coherence with the pressure fluctuations. The corresponding contours are shown for individual frequency components. The coherence estimation technique was similar to the one used in Sec. III C, wherein the time series was divided in two segments with 454 samples each. The corresponding frequency resolution is  $\Delta St \approx 0.03$ . In this case, the second frequency component  $St = 0.12$  lies close to the dominant frequency obtained from the spectrum in Fig. 14. The first frequency component is similar to the one used in Fig. 12. Limiting streamlines and the  $c_{f_x} = 0$  contour are shown on the floor and left sidewall using solid black and white lines, respectively. The contours of mean density (shown in Fig. 4) on the ramp-normal plane as well as the locations of mean separation and reattachment are also included. The corresponding contour labels are not shown to reduce clutter.

Figure 15(a) shows the trend of coherence magnitude for the lowermost frequency component  $St = 0.03$ . The separation bubble breathing shows a strong linear relationship with events inside the separated zone (indicated by the  $c_{f_x} = 0$  contour) as expected. The coherence magnitude decreases along the span, both towards the left and right sidewalls. It is significantly lower along the intermittent length of the shock oscillations [compare with Fig. 12(a)]. On the left sidewall, moderate to high values of coherence (in green) are observed within and close to sidewall separation, based on the  $c_{f_x} = 0$  contour. Therefore, it seems that the breathing motion of sidewall separation zones, hypothesized in Sec. III C, are affected by the dynamics of centerline separation. On the ramp-normal plane, the  $\lambda$ -shock structure is characterized by low values of coherence. The region between the shock system and ramp surface is well correlated with the separation bubble motion. On the center plane in Fig. 15(b), the trace along the compression ramp shock is characterized by low-coherence magnitudes, suggesting a weak correlation between shock oscillations and breathing

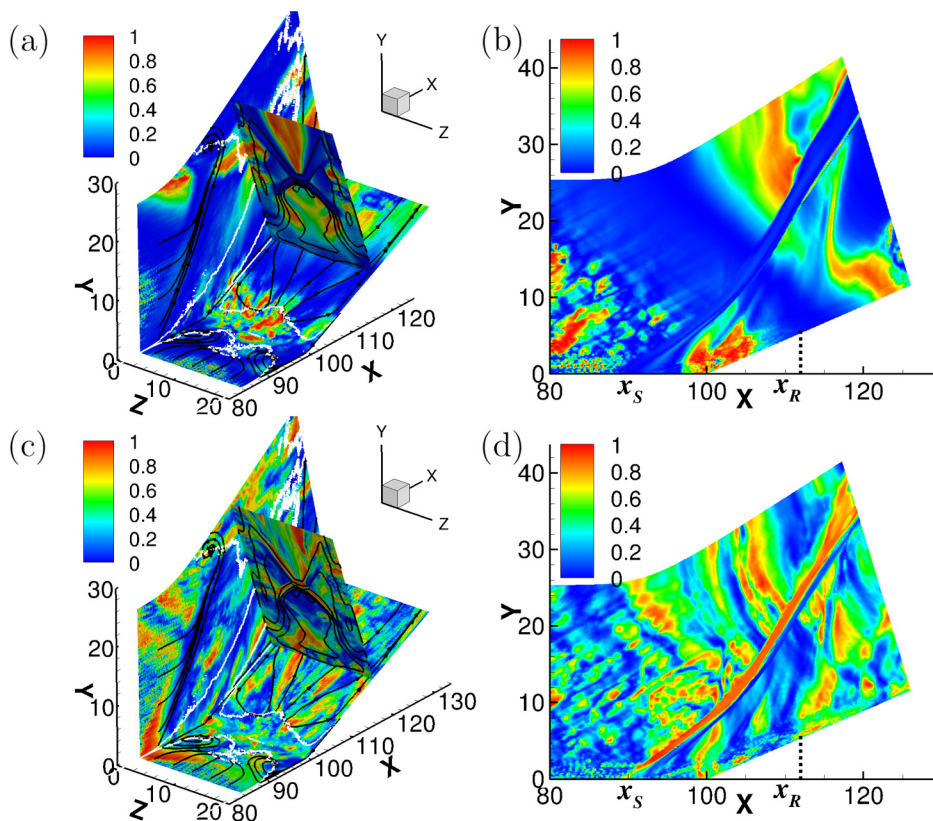


FIG. 15. Coherence of oscillations of centerline separation bubble with pressure fluctuations for (a), (b)  $St = 0.03$ , (c), (d)  $St = 0.12$ . In (a) and (c), the solid black and white lines on the floor and left sidewall represent the limiting streamlines and  $c_{fx} = 0$  contour, respectively. Solid black lines on the ramp-normal plane indicate the mean density contours. Solid and dashed black lines on the center plane in (b) and (d) indicate the mean dividing streamline ( $u/U_\infty = 0$ ) and the sonic line, respectively.

motion of the separation bubble at this particular frequency. On the other hand, high coherence magnitudes are present within the centerline separation.

In case of  $St = 0.12$  shown in Fig. 15(c), the coherence magnitude increases along the intermittent length, closely resembling the band of high coherence observed in Fig. 12. This result indicates the response of the centerline shock to bubble oscillations at the dominant frequency. Within the separated region on the floor, the coherence magnitude is comparatively lower for this component. Post reattachment, streaks of high coherence approximately aligned with the streamlines on the ramp surface are observed. These streaks are most likely a manifestation vortical structures shed from the bubble. On the left sidewall, a small region along the trace of the sidewall shock foot oscillations, lying close to the floor, is distinguished by high values of coherence. The  $\lambda$ -shock structures on the ramp-normal plane are characterized by similar regions. Hence, from these observations, it can be said that the bubble oscillations at this frequency partly drive the motion of the shock front. On the center plane in Fig. 15(d), the motion of the compression ramp shock shows a strong linear relationship with the separation bubble breathing motion, suggesting that the latter drives the former at this frequency.

The coherence plot in Fig. 12 suggested an asymmetric back and forth motion of the interaction, most likely occurring at low frequency. From Fig. 14, the frequencies corresponding to bubble breathing and shock motion are concentrated at frequencies  $St \leq 0.21$ . Hence, to visualize the

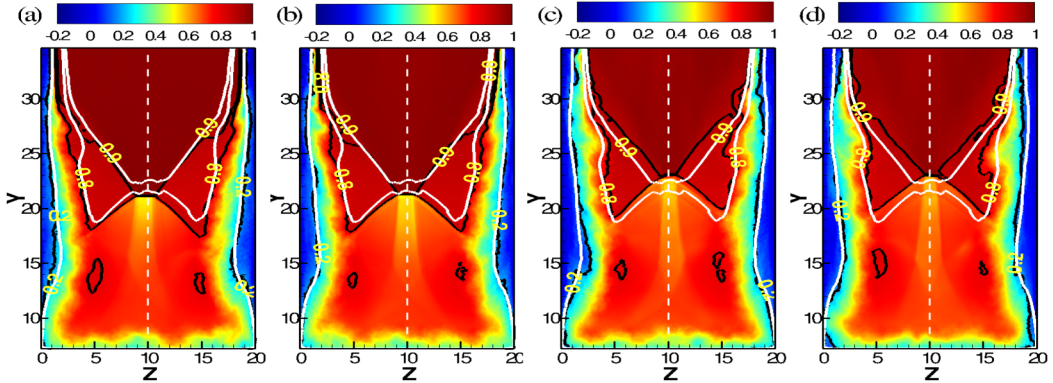


FIG. 16. Contours of low-pass filtered streamwise velocity field ( $u/U_\infty$ ) on the ramp-normal plane at (a)  $t \approx 145 \mu\text{s}$ ; larger right separation bubble (b)  $t \approx 332 \mu\text{s}$ ; mean location and equilibrium (c)  $t \approx 798 \mu\text{s}$ ; larger left separation bubble (d)  $t \approx 871 \mu\text{s}$ ; mean location and equilibrium. Black and white solid lines indicate instantaneous and mean contour levels of  $u/U_\infty = 0.2, 0.8, \text{ and } 0.9$ , respectively. The animation is included as Supplemental Material in Ref. [43].

motion suggested by the coherence plots, a movie of low-pass filtered velocity field was made (see Ref. [43]). A box filter with a cutoff frequency of  $St = 0.21$  was used for this purpose. The movies clearly highlighted the spanwise motion of the interaction caused due to alternate breathing motions of the separation bubbles on the left and right sidewalls. Four clips from the movie are shown in Fig. 16.

In this figure, the contours of instantaneous streamwise velocity are shown on the ramp-normal plane at  $X \approx 116$ . The instantaneous contour levels  $u/U_\infty = 0.2$  (C1),  $0.8$  (C2), and  $0.9$  (C3) are highlighted using black solid lines, with the appropriate labels included. In order to describe the bubble expansion and contraction process, the mean contour levels (shown as white solid lines) corresponding to the aforementioned values are also included. The spanwise center ( $Z = 10$ ) is shown as a white dashed line.

The contour levels  $u/U_\infty = 0.2$  are assumed to be the upper boundary of the sidewall separation bubbles. On the other hand, the contour levels  $u/U_\infty = 0.8$  and  $0.9$  are considered to represent the separation and reattachment shock foot, respectively. Figure 16(a) shows the expansion of the separation bubble on the right sidewall. Notice that the instantaneous contour level C1 lies above its mean counterpart. This expansion motion is associated with the dilation of the separation bubble on the left sidewall. Hence, the interaction moves effectively towards the left and the resulting asymmetry is manifested across the dashed centerline. The instantaneous  $\lambda$ -shock structures lie below their respective mean locations. In Fig. 16(b), the separation bubbles on the sidewalls are approximately at their mean location.

Figure 16(c) shows the expansion process of the separation bubble on the left sidewall. The interaction moves effectively towards the right, while the separation bubble on the right sidewall contracts below the contour level C1. At this instant, the instantaneous  $\lambda$ -shock structures move above their respective mean locations, possibly as a result of downstream movement of the interaction. The interaction returns to the mean position again in Fig. 16(d). The movement of the  $\lambda$ -shock structures seems to be affected by the breathing motion of sidewall-separated regions. Also, another interesting feature observed in the movies is the presence of localized regions of nondimensional velocity with magnitude  $\geq 0.8$ . These regions are present approximately in the range  $10 \leq Y \leq 15$ , at spanwise locations  $Z \approx 5, 15$ . Based on Fig. 3, these regions are most likely representative of tornado vortices emanating from the focus points  $F_1$  and  $F_2$ , respectively (see Fig. 3).

To investigate the influence of events originating within the separation bubble in this interaction, space-time correlations of the mass history of the separation bubble and the shock position histories

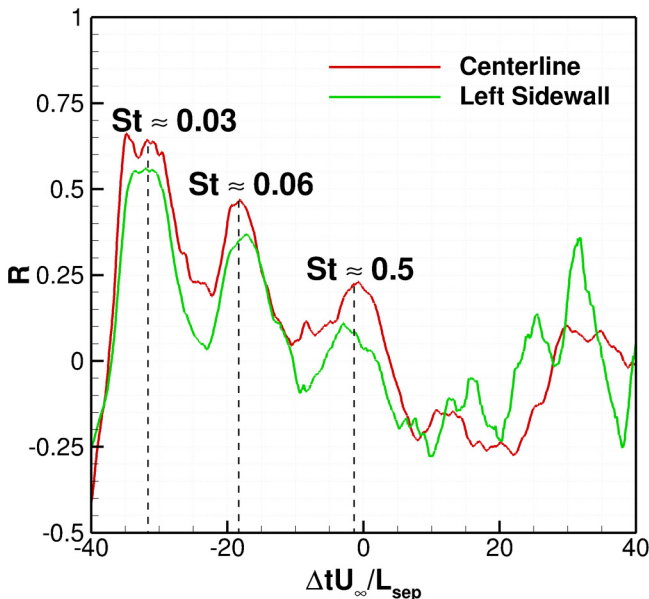


FIG. 17. Space-time correlation of centerline shock oscillations and separation bubble breathing.

at the centerline and left sidewall juncture were carried out. Similar to Figs. 8(b) and 13, the time delay is nondimensionalized by  $L_{\text{sep}}$  and  $U_{\infty}$ . Its reciprocal translates to the Strouhal number. The correlation plots are shown in Fig. 17.

The correlation estimates were calculated without the process of segment averaging in order to resolve higher timescales. The trend of the correlation curves is almost identical for both the shock location histories. Multiple peaks are observed at negative values of time delay ( $\Delta t U_{\infty} / L_{\text{sep}} \approx -32, -18, \text{ and } -2$ ) indicating that an event in the time history of separation bubble mass precedes a similar event in the time history of shock motion. The corresponding Strouhal numbers are representative of low-frequency shock oscillations ( $St \approx 0.03, 0.06$ ) and vortex shedding from the separated shear layer ( $St \approx 0.5$ ). A local peak occurs at a positive value ( $\Delta t U_{\infty} / L_{\text{sep}} \approx 32$ ,  $St \approx 0.03$ ) of time delay which suggests that certain shock motions trigger the motion of the separation bubble. These observations agree with the results of Dupont *et al.* [44,45], Piponniau *et al.* [46], and Wu and Martin [41].

### E. Coupling between centerline, corner, and sidewall interactions

This section investigates the extent to which the dynamics of the centerline separation affects the corner and sidewall interactions. Previous studies on confined SWTBLI [17,18] have examined the spanwise variation of two-point correlations of wall-pressure fluctuations in the vicinity of the mean separation line. Rabey *et al.* [17] analyzed the flow field associated with a reflecting SWTBLI with a confinement ratio  $\delta/w = 0.069$ . They observed that when the reference point was located at the centerline, the correlations diminished beyond 20% of the half-span. When the reference point was moved towards the sidewalls, the correlation magnitudes decreased beyond the foci. Based on these results, they concluded that the corner and centerline separations did not influence each other significantly.

Poggie and Porter [18] carried out a similar procedure in case of a compression ramp with a confinement ratio  $\delta/w = 0.12$ . When the reference point was located at the centerline, high correlation magnitudes persisted up to the sidewall, indicating a relationship between the centerline and corner separations. This is caused by a higher confinement ratio, which translates to higher

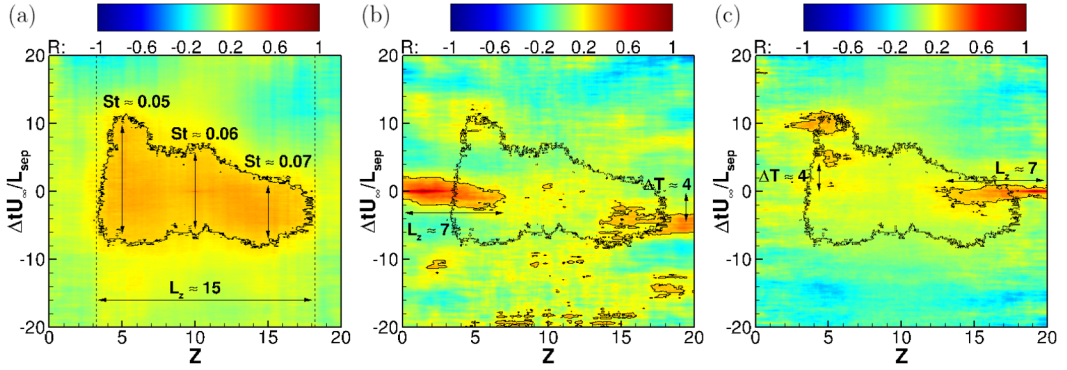


FIG. 18. Space-time correlations with reference point at  $X \approx 92$  and (a) at the centerline ( $Z = 10$ ), (b) close to the left sidewall ( $Z \approx 1.5$ ), and (c) close to the right sidewall ( $Z \approx 19.2$ ). Solid lines represent the  $R = 0.25$  contour level. Dotted lines in (b) and (c) represent the  $R = 0.25$  contour level in (a).

three dimensionality in the flow field. On moving the reference point towards the sidewalls, the resulting correlation plot showed no indication of affecting the centerline separation. High correlation magnitudes were localized, thereby suggesting response local events such as asymmetric back-and-forth motion of the interaction or passing of corner vortices.

For the same case, space-time correlations of wall-pressure fluctuations are shown in Fig. 18. Segment averaging over an ensemble of two signals (with 454 samples each) was used to calculate the correlation estimates. The spanwise variation of correlations is examined at  $X \approx 92$ , which lies close to the mean separation line. Time delay plotted on the  $y$  axis is scaled by  $U_\infty$  and  $L_{sep}$ . The spanwise coordinates are shown on the  $x$  axis. Following the approach by Rabey *et al.* [17], the contour levels lying in the range  $-0.2 < R < 0.2$  are suppressed to mitigate noise.

Figure 18(a) illustrates the correlations with the reference point located at the centerline. Using the threshold mentioned earlier, the extent of well-correlated region is  $L_z \approx 15$ , covering 75% of the span. Starting from the left, the width of this well-correlated region decreases across the span. Physically, it represents the timescale of an event at a particular location. The Strouhal number(s) across the span range from  $0.05 \leq St \leq 0.07$ , indicating that the pressure fluctuations are caused by the low-frequency shock oscillations. In Fig. 18(b), when the reference point is moved towards the left sidewall ( $Z \approx 1.5$ ), the length of the well-correlated region ( $L_z$ ) is  $\approx 7$ , thereby covering about 35% of the span. The corresponding region is roughly elliptical in shape. The Strouhal numbers calculated from the width lie in the range  $0.25 \leq St \leq 0.33$ . At the right sidewall ( $Z \approx 20$ ), a similar well-correlated region occurs at a nondimensional time delay  $\Delta T \approx 4$ . Since this region occurs at a negative value, the event at the left sidewall is preceded by a similar event at the right sidewall. Based on the Strouhal number ( $St \approx 0.25$ ), these events most likely correspond to the alternate passing of the corner vortices.

The well-correlated region delineated by the  $R = 0.25$  contour level in Fig. 18(a) is also included in this figure. Notice that there is a significant overlap between the well-correlated regions in Figs. 18(a) and 18(b), suggesting that the dynamics of corner separation at the left sidewall extend well into the domain affected by the dynamics of centerline separation. This trend is repeated in Fig. 18(c), wherein the reference point is located close to the right sidewall. The spanwise extent and shape of the well-correlated region is same as the one in Fig. 18(b), and similar events at the right sidewall occur at the same nondimensional time delay  $\Delta T \approx 4$ .

Figure 19 illustrates the plots of space-time correlations which determine the relationship between the centerline and sidewall interactions. For the plot shown in Fig. 19(a), the reference signal was constructed using pressure fluctuations extracted on the floor at  $(X, Z) = (90.2, 10)$ . This signal is correlated with pressure fluctuations on the left sidewall along various wall-normal locations, at

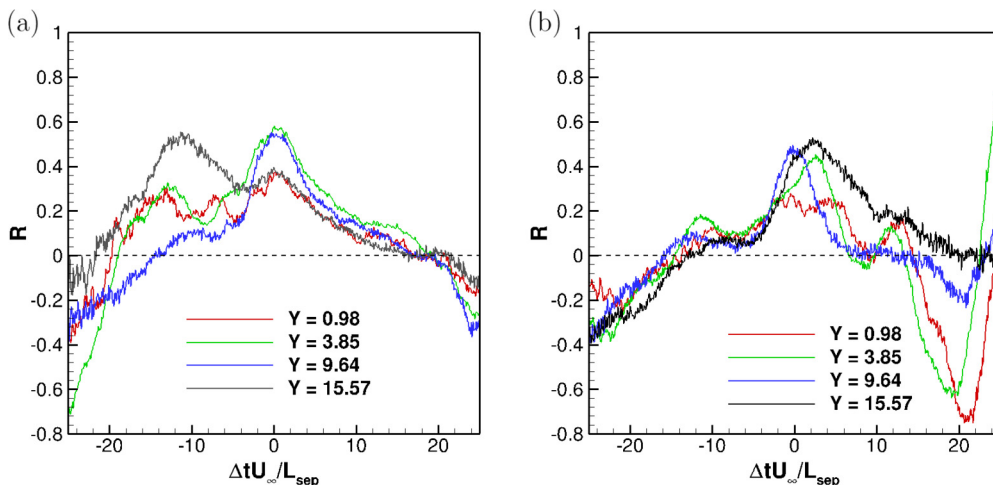


FIG. 19. Space-time correlation between (a) pressure fluctuations on the centerline and left sidewall, (b) pressure fluctuations on the left and right sidewalls.

the same streamwise station. In case of Fig. 19(b), the reference signal was composed of pressure fluctuations at  $(X, Y) = (90.2, 8.55)$ . It was then correlated with pressure fluctuations on the right sidewall along various wall-normal locations at the same streamwise location. The correlation estimates were calculated by averaging over an ensemble of two signals with 454 samples each. The nondimensional time delay used in the previous figure is plotted on the  $x$  axis and the correlation magnitude is shown on the  $y$  axis.

Figure 19(a) determines the relationship between interactions at the centerline and on the left sidewall. For all the cases, there exists a broad region of positive correlation, suggesting in-phase pressure fluctuations ( $p'$ ). At  $Y = 0.98$ , this region starts at  $T \approx -19.8$ . Since the time delay is negative, the event first occurs on the left sidewall and is most likely caused by an upstream movement of the corresponding  $\lambda$ -shock structure ( $p' > 0$ ). This event is correlated with a similar upstream movement of the centerline shock ( $p' > 0$ ) after  $\Delta T \approx 19.8$ , leading to a positive correlation. The peak at  $T = 0$  suggests that the centerline shock and  $\lambda$ -shock structure on the left sidewall are at their most upstream location.

For positive time delays, the event first occurs at the centerline. Downstream movement of the centerline shock leads to the drop in correlation magnitude. At  $T \approx 17$ , the correlation plot switches signs as the centerline shock moves downstream of the reference station ( $p' < 0$ ), while the  $\lambda$ -shock structure is still upstream ( $p' > 0$ ). A valley is expected to occur either at the edge of the correlation plot ( $T = 25$ ) or beyond it. This particular feature is representative of the centerline shock at its most downstream location. The elapsed time between when the centerline shock is at its most upstream location (at  $T = 0$ ) and when it reaches its most downstream location ( $T = 25$ ) translates to a Strouhal number of  $St = 1/\Delta T = 0.04$ . This value corresponds to the centerline shock oscillation frequency and is consistent with the spectrum in Fig. 11. In presence of a longer window segment that resolves higher values of time delay, the correlation plot can be expected to trend towards positive value as the  $\lambda$ -shock structure on the left sidewall would have moved downstream of the reference station ( $p' < 0$ ), while the centerline shock is still downstream of its mean but is translating upstream.

This trend persists at  $Y = 3.85$ , but changes slightly at  $Y = 9.64$ . For this case, upstream motion of the left sidewall  $\lambda$ -shock structure occurs later at  $T = -13.67$  since at this height, it is farther away from the reference station (along the streamwise direction). Again, the plot peaks at  $T = 0$ . Interestingly, this upstream movement occurs earliest at  $Y = 15.57$ . A possible explanation for this can be attributed to an increased separation extent at higher heights, due to the nature of swept



interactions. This in turn causes the separation shock foot (within the  $\lambda$ -shock structure) to reach the corresponding reference station earlier. Notice that for all wall-normal locations, the valley occurs at approximately the same value of positive time delay.

Figure 19(b) inspects the relationship between the interactions on the left and right sidewalls. As mentioned previously, the reference signal for this case was extracted at  $(X, Y) = (90.2, 8.55)$  on the left sidewall. At negative time delays, the event occurs first on the right sidewall. At  $Y = 0.98$ , it seems that the plot switches sign to negative values at some value of time delay  $< -25$ . This instant can be interpreted as the  $\lambda$ -shock structure on the right sidewall moving downstream of its reference station ( $p' < 0$ ), while that on the left sidewall moving upstream ( $p' > 0$ ). The valley at  $T \approx -20$  corresponds to the  $\lambda$ -shock structure on the right sidewall at its most downstream location and beginning its upstream motion. This confirms the asymmetric motion deduced from the coherence plots in Fig. 12. Poggie and Porter [18] carried out conditional averaging in their analysis of the same flow field, which highlighted similar asymmetric motions. (See Figs. 16 and 17 in that reference.)

At  $T = -13.75$ , the right sidewall shock structure moves upstream of the reference station ( $p' > 0$ ). The resulting region of positive correlation peaks at  $T = 0$  and extends up to  $T = 14.28$ . Note that at positive time delays, any particular event occurs first on the left sidewall. The latter may correspond to a downstream movement of the left sidewall shock structure ( $p' < 0$ ). A valley occurs at  $T \approx 20$ , after which the plot immediately switches back to positive values of correlation at  $T = 24.45$ , possibly caused by downstream movement of the right sidewall shock structure. At this instant, both the shock structures lie downstream of their respective reference stations. Considering the shock structure on the right sidewall, the elapsed time between its upstream (at  $T = -13.75$ ) and downstream movement (at  $T = 24.45$ ) is 38.2. This translates to a Strouhal number of  $\approx 0.026$ , which is a representative frequency scale of the asymmetric motion of sidewall interactions described earlier in the paper.

#### IV. CONCLUSIONS

Statistical analysis of results obtained from the simulations of Poggie and Porter [18] was carried out. The mean and instantaneous flow fields highlighted curving of the shock front due to sidewall effects. Based on the skin-friction contours, flow at the corner separated at a location upstream relative to the separation at the centerline. Critical point analysis on the floor suggested the presence of tornado vortices originating at foci close to the sidewalls. An interaction similar to that produced by a sharp fin was observed on the sidewalls with a  $\lambda$ -shock foot and separation vortex. The separation extent on the sidewalls increased downstream. A vortex system comprised of a pair of corner vortices, a horseshoe vortex, and swept sidewall vortices was observed from the mean density contours. Peak values of RMS pressure fluctuations were observed downstream of mean reattachment on the floor. Based on the instantaneous contours, this was attributed to the reflection of sidewall  $\lambda$ -shock structures at that location.

Spectra of pressure fluctuations for individual frequency components were plotted on the sampled surfaces. For the lowest-frequency component ( $St = 0.03$ ), the spectra highlighted the intermittent length of the shock motion on both the floor and sidewalls. The locations corresponding to the sidewall  $\lambda$ -shock feet were comprised of high values of spectral energy density, which confirmed low-frequency oscillations of the same. At mid frequencies ( $St = 0.12$ ), regions in the vicinity of foci on the floor showed an increase in the spectral energy density. At higher frequencies ( $St = 0.36$ ), zones within the centerline separation on the floor and separation vortex on the sidewalls were energy dominant. Similar plots on the center plane characterized the low-frequency shock motion (at  $St = 0.03$ ) and shedding of horseshoelike vortices (at  $St = 0.12$ ) originating at the focus within the centerline separation. At higher frequencies, spectral energy was concentrated in the separated shear layer, local compression waves, and in the separation zone close to the reattachment.

The shock location histories at the centerline and left juncture were extracted using a pressure-based sensor and the corresponding spectra displayed peaks in the low-frequency range. The influence of sidewalls on the flow-field unsteadiness was investigated using coherence and

correlations. Initially, the time history of the centerline shock location was used to calculate coherence with pressure fluctuations in the domain. The corresponding contours were plotted for the lowest-frequency components ( $St = 0.03$  and  $0.06$ ). For  $St = 0.03$ , the shock oscillations showed a strong linear relationship with pressure fluctuations within the intermittent length on the floor and sidewall, as well as with the  $\lambda$ -shock structure on the sidewalls. This band of high coherence on the floor was skewed in the upstream direction towards the left sidewall, which suggested alternate back and forth movement of the sidewall interactions at lower frequencies. The authors attribute this to the breathing motion of the concomitant-separated regions that are out of phase, but a more rigorous analysis is warranted. The spectrum of separation bubble breathing highlighted a dominant frequency component at  $St \approx 0.11$ . Based on the coherence and correlation plots, this component partly drives the centerline shock oscillations at this frequency. The breathing motion of the centerline separation bubble at lower frequencies seems to have a localized effect, with no significant relationship with the events on the sidewall. The low-pass filtered velocity fields indicated spanwise motion of the interaction (possibly caused by alternating breathing motion of the separated regions on the sidewalls), in addition to the back-and-forth streamwise motion.

Space-time correlations of wall-pressure fluctuations on the floor were carried out to determine the influence of centerline separation on those at the corners and sidewalls. The domain of influence of centerline separation encompassed 75% of the span. The corresponding timescale(s) calculated from the width of the well-correlated region lay in the low-frequency range, signifying the presence of shock motion. The domain of influence for corner separations at either juncture extended up to 35% of the span and lay well within the bounds of the centerline separation. Corner separation at one end affected the other after a time delay, which physically may correspond to the transport of fluid in the spanwise direction. A similar exercise was carried out to investigate the relationship between interactions at the centerline and on the sidewalls. The resulting correlations confirmed the asymmetric motion of the sidewall interactions occurring at  $St \approx 0.026$ , as indicated by the coherence plots as well as the low-pass filtered velocity fields.

#### ACKNOWLEDGMENTS

This work was supported in part by the U.S. Air Force Office of Scientific Research Grant No. FA9550-17-1-0153, monitored by I. Leyva. Computer time was provided by Purdue University's Rosen Center for Advanced Computing. The original computation was supported by the DOE INCITE Program. This research used resources of the Argonne Leadership Computing Facility, which is a DOE Office of Science User Facility supported under Contract No. DE-AC02-06CH11357.

- 
- [1] J. E. Green, Interactions between shock waves and turbulent boundary layers, *Prog. Aerosp. Sci.* **11**, 235 (1970).
  - [2] D. S. Dolling, Fifty years of shock-wave/boundary-layer interaction research: What next? *AIAA J.* **39**, 1517 (2001).
  - [3] N. T. Clemens and V. Narayanaswamy, Low-frequency unsteadiness of shock wave/turbulent boundary layer interactions, *Annu. Rev. Fluid Mech.* **46**, 469 (2014).
  - [4] D. V. Gaitonde, Progress in shock wave/boundary layer interactions, *Prog. Aerosp. Sci.* **72**, 80 (2015).
  - [5] J. W. Nichols, J. Larsson, M. Bernardini, and S. Pirozzoli, Stability and modal analysis of shock/boundary layer interactions, *Theor. Comput. Fluid Dyn.* **31**, 33 (2017).
  - [6] M. C. Adler and D. V. Gaitonde, Dynamic linear response of a shock/turbulent-boundary-layer interaction using constrained perturbations, *J. Fluid Mech.* **840**, 291 (2018).
  - [7] D. C. Reda and J. D. Murphy, Shock wave/turbulent boundary-layer interactions in rectangular channels, *AIAA J.* **11**, 139 (1973).
  - [8] D. C. Reda and J. D. Murphy, Sidewall boundary-layer influence on shock wave/turbulent boundary-layer interactions, *AIAA J.* **11**, 1367 (1973).

- [9] P. J. K. Bruce, D. M. F. Burton, N. A. Titchener, and H. Babinsky, Corner effect and separation in transonic channel flows, *J. Fluid Mech.* **679**, 247 (2011).
- [10] D. M. F. Burton and H. Babinsky, Corner separation effects for normal shock wave/turbulent boundary layer interactions in rectangular channels, *J. Fluid Mech.* **707**, 287 (2012).
- [11] X. Xiang and H. Babinsky, Corner effects for oblique shock wave/turbulent boundary layer interactions in rectangular channels, *J. Fluid Mech.* **862**, 1060 (2019).
- [12] W. E. Eagle and J. F. Driscoll, Shock wave–boundary layer interactions in rectangular inlets: Three-dimensional separation topology and critical points, *J. Fluid Mech.* **756**, 328 (2014).
- [13] M. Funderburk and V. Narayanaswamy, Experimental investigation of primary and corner shock boundary layer interactions at mild back pressure ratios, *Phys. Fluids* **28**, 086102 (2016).
- [14] E. Garnier, Stimulated detached eddy simulation of three-dimensional shock/boundary layer interaction, *Shock Waves* **19**, 479 (2009).
- [15] N. Bisek, *Sidewall Interaction of a Supersonic Flow over a Compression Ramp*, AIAA Paper 2015–1976 (American Institute of Aeronautics and Astronautics, Kissimmee, FL, 2015).
- [16] B. Wang, N. D. Sandham, Z. Hu, and W. Liu, Numerical study of oblique shock-wave/boundary-layer interaction considering sidewall effects, *J. Fluid Mech.* **767**, 526 (2015).
- [17] P. K. Rabey, S. P. Jammy, P. J. K. Bruce, and N. D. Sandham, Two-dimensional unsteadiness map of oblique shock wave/boundary layer interaction with sidewalls, *J. Fluid Mech.* **871**, R4-1 (2019).
- [18] J. Poggie and K. M. Porter, Flow structure and unsteadiness in a highly confined shock-wave–boundary-layer interaction, *Phys. Rev. Fluids* **4**, 024602 (2019).
- [19] M. Tobak and D. J. Peake, Topology of three-dimensional separated flows, *Annu. Rev. Fluid Mech.* **14**, 61 (1982).
- [20] R. R. Morajkar, R. L. Klomparens, W. E. Eagle, J. F. Driscoll, M. Gamba, and J. A. Benek, Relationship between intermittent separation and vortex structure in a three-dimensional shock/boundary-layer interaction, *AIAA J.* **54**, 1862 (2016).
- [21] I. Bermejo-Moreno, L. Campo, J. Larsson, J. Bodart, D. Helmer, and J. K. Eaton, Confinement effects in shock wave/turbulent boundary layer interactions through wall-modelled large-eddy simulations, *J. Fluid Mech.* **758**, 5 (2014).
- [22] D. Lushner and N. Sandham, The effect of flow confinement on laminar shock-wave/boundary-layer interactions, *J. Fluid Mech.* **897**, A18 (2020).
- [23] A. E. Perry and H. Hornung, Some aspects of three-dimensional separation. II. Vortex skeletons, *Z. Flugwiss. Weltraumforsch.* **8**, 155 (1984).
- [24] M. R. Visbal and D. V. Gaitonde, *Shock Capturing Using Compact-Differencing-Based Methods*, AIAA Paper 2005–1265 (American Institute of Aeronautics and Astronautics, Reston, VA, 2005).
- [25] W. K. Anderson, J. L. Thomas, and B. Van Leer, Comparison of finite volume flux vector splittings for the Euler equations, *AIAA J.* **24**, 1453 (1986).
- [26] J. Poggie, N. J. Bisek, and R. Gosse, Resolution effects in compressible, turbulent boundary layer simulations, *Comput. Fluids* **120**, 57 (2015).
- [27] J. S. Bendat and A. G. Piersol, *Random Data: Analysis and Measurement Procedures*, 4th ed. (Wiley, Hoboken, NJ, 2010).
- [28] J. M. Détery, R. Legendre and H. Werlé: Toward the elucidation of three-dimensional separation, *Annu. Rev. Fluid Mech.* **33**, 129 (2001).
- [29] A. S. Deshpande and J. Poggie, Flow control of swept shock-wave/boundary-layer interaction using plasma actuators, *J. Spacecr. Rockets* **55**, 1198 (2018).
- [30] A. E. Perry and M. S. Chong, A description of eddying motions and flow patterns using critical-point concepts, *Annu. Rev. Fluid Mech.* **19**, 125 (1987).
- [31] B. Edney, Anomalous Heat Transfer and Pressure Distributions on Blunt Bodies at Hypersonic Speeds in the Presence of an Impinging Shock, Technical Report, Flygtekniska Forsöksanstalten, Stockholm, Sweden, 1968 (unpublished).
- [32] B. Ganapathisubramani, N. Hutchins, W. T. Hambleton, E. K. Longmire, and I. Marusic, Investigation of large-scale coherence in a turbulent boundary layer using two-point correlations, *J. Fluid Mech.* **524**, 57 (2005).

- [33] B. Ganapathisubramani, N. Clemens, and D. Dolling, Effects of upstream boundary layer on the unsteadiness of shock-induced separation, *J. Fluid Mech.* **585**, 369 (2007).
- [34] S. Beresh, N. Clemens, and D. Dolling, Relationship between upstream turbulent boundary-layer velocity fluctuations and separation shock unsteadiness, *AIAA J.* **40**, 2412 (2002).
- [35] K. Porter and J. Poggie, Selective upstream influence on the unsteadiness of a separated turbulent compression ramp flow, *Phys. Fluids* **31**, 016104 (2019).
- [36] S. Pirozzoli and F. Grasso, Direct numerical simulation of impinging shock wave/turbulent boundary layer interaction at  $M = 2.25$ , *Phys. Fluids* **18**, 065113 (2006).
- [37] L. Agostini, L. Larchevêque, and P. Dupont, Mechanism of shock unsteadiness in separated shock/boundary-layer interactions, *Phys. Fluids* **27**, 126103 (2015).
- [38] M. Grilli, P. J. Schmid, S. Hickel, and N. A. Adams, Analysis of unsteady behavior in shockwave turbulent boundary layer interaction, *J. Fluid Mech.* **700**, 16 (2012).
- [39] F. O. Thomas, C. M. Putnam, and H. C. Chu, On the mechanism of unsteady shock oscillation in shock wave/turbulent boundary layer interactions, *Exp. Fluids* **18**, 69 (1994).
- [40] S. Priebe and M. P. Martín, Low-frequency unsteadiness in shock wave–turbulent boundary layer interaction, *J. Fluid Mech.* **699**, 1 (2012).
- [41] M. Wu and M. P. Martin, Analysis of shock motion in shockwave and turbulent boundary layer interaction using direct numerical simulation data, *J. Fluid Mech.* **594**, 71 (2008).
- [42] V. Pasquariello, S. Hickel, and N. A. Adams, Unsteady effects of strong shock-wave/boundary-layer interaction at high reynolds number, *J. Fluid Mech.* **823**, 617 (2017).
- [43] See Supplemental Material at <http://link.aps.org/supplemental/10.1103/PhysRevFluids.6.024610> for the animation of low-pass filtered streamwise velocity field, describing the motion of the sidewall separated zones.
- [44] P. Dupont, C. Haddad, and J. F. Debiève, Space and time organization in a shock-induced separated boundary layer, *J. Fluid Mech.* **559**, 255 (2006).
- [45] P. Dupont, S. Piponniau, A. Sidorenko, and J. F. Debiève, Investigation by particle image velocimetry measurements of oblique shock reflection with separation, *AIAA J.* **46**, 1365 (2008).
- [46] S. Piponniau, J. P. Dussauge, J. F. Debiève, and P. Dupont, A simple model for low-frequency unsteadiness in shock-induced separation, *J. Fluid Mech.* **629**, 87 (2009).